Number Density Distribution of Satellite Galaxies around Massive Central Galaxies in CLAUDS + HSC at $0.3 < z < 0.9$

by

Lingjian Chen

A Thesis Submitted to Saint Mary's University, Halifax, Nova Scotia in Partial Fulfillment of the Requirements for the Degree of Master of Science in Astronomy (Department of Astronomy and Physics)

August 2019, Halifax, Nova Scotia

Approved: _____
Dr. Marcin Sawicki
Supervisor

Approved: _____
Dr. Ivana Damjanov
Examiner

Approved: _____
Dr. Robert Thacker
Examiner

Date: August 19th, 2019.

Acknowledgements

First of all, I want to thank my supervisor Dr. Marcin Sawicki, for guiding me through the project and teaching me what it takes to do great research. Thanks to Thibaud and Anneya for putting together such a good dataset for me to analyze. I also want to thank Dr. Ivana Damjanov for discussion and constructive suggestions, and for that I thank other members from the CLAUDS team as well.

Thanks to all my fellow grad students, especially Nathalie for many pieces of advice on how to survive grad school. I also thank all the faculty members and our secretary Florence for helps when I needed them.

I am very grateful for my parents, as they have been very supportive all the time, and encouraged me to pursue a career that I like. Last but not least, I thank my friends, they have given me strength to carry on during this quite intensive and difficult two years.

Contents

List of Figures

List of Tables

Abstract

Number Density Profiles of Satellite Galaxies around Massive Central Galaxies in CLAUDS + HSC at $0.3 < z < 0.9$

by Lingjian Chen

Satellite galaxies around massive central galaxies can provide important information about galactic environmental effect. In this thesis, we selected thousands of massive ($\log(M_{cen}/M_{\odot}) > 11.15$) central galaxies using wide and deep imaging data at $0.3 < z < 0.9$ and investigated radial number density distribution of the satellites. The distribution of satellites can be described by the NFW profile at large projected radii but deviates from it in inner regions (within $\sim$100 kpc). We found that low-massive satellite galaxies ($9.5 < \log(M_{sat}/M_{\odot}) < 10.2$) have more significant deviation from the NFW than high-mass ($\log(M_{sat}/M_{\odot}) > 10.2$). For central galaxy dependence, we found galaxy conformity signal and that the number of satellites increases with central mass. Redshift evolution enhances number density in inner regions more significantly than in outer regions. We propose that shape of the satellite distribution is related to migration, involving effects such as dynamical friction and tidal stripping. We compared our results with the IllustrisTNG simulation.

August 19th, 2019

Chapter 1

Introduction

1.1 Environmental Effect on Galaxy Evolution

The Universe now contains large scale structure (LSS) which originates from the initial fluctuations in the density field immediately after the Big Bang. Galaxies were born is this structure following the density distribution in the LSS. The LSS now has a node-filament-void feature, known as the cosmic web (Trujillo et al. 2006; Sarkar & Pandey 2019). The nodes in the LSS are the most dense regions in the Universe where galaxy clusters were formed, and the clusters accrete matter from the filaments where matter is less dense.

Galaxies are essential building blocks of the Universe which contain baryonic matter (stars, gas and dust) and dark matter. The study of galaxy evolution is not only useful for testing the physics of galaxy formation but is also exploring formation of larger structures.

Galaxies evolve through cosmic time by many internal (secular evolution) or external mechanisms. The existence of external mechanisms such as encounters, mergers and interaction with the intergalactic medium significantly complicates the study of galaxy evolution. This is the environmental effect (e.g., Boselli & Gavazzi 2006; Weinmann et al. 2009). In an isolated situation, galaxies evolve collectively due to internal mechanisms such as star formation, gas consumption and feedback processes (e.g., Mo et al. 2010). During their evolution process, the galaxies may go through morphological changes, metallicity changes and other transformations due to its internal processes. However, in a dense environment, various external mechanisms related to interactions between galaxies and their dark matter halo may be present, which can significantly modify their evolution path.

In the rest of this chapter, I will introduce the current knowledge of the environmental effects on galaxy evolution from theoretical and observational aspects. We assume WMAP9 cosmology (Hinshaw et al. 2013, $H_0 = 69.3$ km/s/Mpc, $\Omega_m = 0.287$) throughout the thesis.

1.1.1 Theoretical Arguments

Although astronomers now have a fairly good idea of how to model galaxy evolution if the galaxies are isolated(e.g., Somerville & Davé 2015), galaxy evolution under environmental influence is less known. Various studies (e.g. Balogh et al. 2004; Weinmann et al. 2006; Fossati et al. 2017; Moutard et al. 2018) have shown that environmental effects play important roles in the evolution of galaxies (e.g. environmental quenching and stripping

of matter). Environmental effects are expected to be the strongest in the most dense regions such as galaxy clusters, but should still be quite visible in less rich galaxy groups (Gómez-Guijarro et al. 2018; Hashimoto et al. 1998; Wetzel et al. 2012).

In the mass budget of such dense environments, the host dark matter halo is the dominant component, followed by baryonic matter, most of which is in stars and gas reservoir of central and satellite galaxies. The dark matter halo follows a density distribution as described by Navarro et al. (1995) (the Navarro-Frenk-White profile, hereafter NFW profile). Since dark matter contribute most of the mass, it defines the potential well in dense environments and its properties are very important for environmental effects.

For the stellar component that we can directly trace in a dense environment, there is a central galaxy (usually the most massive galaxy) which resides very close to the dynamical center of cluster or group of galaxies. Satellite galaxies are less massive and they are gravitationally bound to the central galaxy on various orbits. Properties of satellite galaxies can be correlated to properties of the central galaxy, and the host dark matter halo, but they do not necessarily have the same properties as the central galaxy or each other. Statistically, they usually have different properties from their field counterparts due to the environment they are in(Balogh et al. 1999; Wetzel et al. 2012).

For satellite galaxies, major environmental mechanisms that can affect galaxy evolution under such conditions include tidal effects, dynamical friction, harassment, ram pressure stripping, etc. Tidal forces (Read et al. 2006; Tollet et al. 2017) come from the fact that dif-

ferent parts of the satellite galaxy experience different strengths of gravitational force from the host potential well. Thus, the tidal force can strip loosely-bound matter that lies in the outskirts of small galaxies with shallow potential wells (mostly the dark matter component gets stripped first because they are more extended, e.g. Niemiec et al. 2017). Dynamical friction (Chandrasekhar 1943; Binney & Tremaine 1987) is a frictional force that decelerates objects that fall in the cluster or group dark matter halo and shrinks the orbit of satellite galaxies. Galaxy harassment arises from the high-speed encounters between the satellite galaxies themselves which acts to strip material from the galaxy and modify its morphology (Moore et al. 1996). Ram pressure (Gunn & Gott 1972; Binney & Tremaine 1987) is generated from dense intracluster medium to a galaxy's gas reservoir when the galaxy travels through it, generating shock waves which can blow the gas reservoir out of the galaxy and quench star formation in the galaxy (ram pressure stripping). All the previously mentioned external mechanisms should be considered all together to modify the matter distribution and the satellite galaxy population, each playing a unique role in processing the satellite galaxies.

Moreover, galaxies are expected to have higher probability of merging in dense regions, because a denser environment means more chances of galaxy encounters. In most dense regions like clusters, the merger rate depends on various properties of the environment and satellite galaxies themselves (Kitzbichler & White 2008; Jiang et al. 2008). These merging events not only change the satellite population, but also change the mass of the central

galaxy, as the mass growth of quiescent central galaxies mainly comes from minor mergers with satellite galaxies.

1.1.2 Observational Evidence of the Environmental Effect

There is also many pieces of convincing observational evidence that supports the argument that galaxy evolution is different in dense environments than in the isolated situation, implying the existence of environmental effects (e.g. Balogh et al. 2004; Weinmann et al. 2006; Fossati et al. 2017; Moutard et al. 2018). In observation, satellite galaxies in dense regions are direct tracers to infer environmental effect on galaxy evolution. The general consensus from observations is that satellites are processed in clusters, confirming the theoretical predictions (Weinmann et al. 2009). Environmental processes tend to quench satellite galaxies and make them lose mass, mostly to the more extended dark matter halo component (e.g. Niemiec et al. 2017).

Galaxies in clusters or groups have different evolutionary paths and properties from field massive galaxies at the same masses (e.g. Niemi et al. 2010; Salerno et al. 2019). Unlike isolated massive galaxies, stellar mass growth for central galaxies in dense environments can be from smaller satellite galaxies merging into them, especially at low redshift (sometimes called galaxy cannibalism, Vulcani et al. 2016). For quiescent central galaxies, this can be the only way they can grow in mass.

The quenched fraction of satellite galaxies is higher in cluster environments (Oemler

1974). Morphology-density relation (Postman & Geller 1984; Dressler et al. 1997) is also a well-known relation in which early-type galaxies are more common in dense environments. Galaxy conformity was first observed in low-redshift in Weinmann et al. (2006), as higher fraction of quiescent satellites around quiescent centrals than around star-forming centrals. This is related to environmental quenching due to external processes as opposed to mass quenching due to internal mechanisms such as stellar feedback or AGN feedback. Some papers also reported that quenched fraction increases toward the cluster center (e.g., Prescott et al. 2011).

Another popular approach to study satellite galaxy behavior in clusters or groups is to study their number density as a function of distance from the central galaxy. The spatial distribution and their properties of satellite galaxies in galaxy clusters or groups can provide crucial information for galaxy evolution in dense environments (e.g. Guo et al. 2012; Chen 2008). For example, environmental quenching of satellite galaxies is an important process in formation of galaxy groups and clusters, one can suspect this effect is greater in the cluster or group cores where galaxy density is higher (e.g. Smith et al. 2012; Guo et al. 2017; Barsanti et al. 2018). The red fraction of satellite galaxies is a feature of quenching and it can provide rich information for environment effect on the satellite galaxies (Prescott et al. 2011; Kovač et al. 2014). The relation between the satellite distribution and the dark matter distribution is also an important feature to look for processes that are particular to baryonic matter. Whether the spatial distribution of satellite galaxies trace underlying

dark matter distribution is a key question for galaxy distribution and its relation to dark matter distribution (Watson et al. 2012; Wang et al. 2018). There are also some additional questions concerning central galaxies in these systems, such as how does mass grow for a central galaxy, how much stellar mass was acquired by star-forming action and how much by accretion and how do these processes depend on galactic environment.

Many studies have examined the spatial distribution of satellites at low-redshift ($z < 0.1$, e.g. Chen 2008; Wang et al. 2014a; Watson et al. 2012; Piscionere et al. 2015), at intermediate redshift ($0.1 < z < 1$,e.g.Tal et al. 2012b; Nierenberg et al. 2012; Prescott et al. 2011) and at higher redshift ($z > 1$, e.g.Kawinwanichakij et al. 2014; Hartley et al. 2015) by looking at radial number density profiles in dense environments around massive central galaxies. Most low-redshift surveys were based on the SDSS survey and high-redshift studies were based on deep surveys which cover small areas. A general consensus is that radial number density of satellite galaxies drops moving away from central galaxy, i.e. satellite galaxy number density is highest at cluster cores (e.g.Chen 2008; Lares et al. 2011; van den Bosch et al. 2005; Hartley et al. 2015). During the past decade, the description of the distribution has been more and more complex and accurate thanks to growing sample size. Chen (2008) calculated radial number density profile for SDSS satellite populations and found that the typical profile can be described by a power law. Budzynski et al. (2012) found the mean number density profile of SDSS DR7 satellites ($0.15 < z < 0.4$) can be well described by an NFW profile. Tal et al. (2012a) additionally found that radial distribution of

satellite galaxies deviates from power-law in inner regions of clusters and are best described by NFW model beyond 25 kpc and additional Sersic profile (Sérsic 1963) within 25 kpc for satellites close to SDSS luminous red galaxies (LRGs). However, this deviation feature has only been seen in low-redshift studies so far.

The dependence of the satellite radial number density distribution on various properties of clusters or groups has also been discussed extensively. Several papers found evidence for the distribution being dependent on satellite stellar mass or luminosity, with more luminous satellites have profiles of steeper slope in low redshift (Watson et al. 2012; Piscionere et al. 2015). A satellite color dependence was also found in multiple studies (e.g., Collister & Lahav 2005; Chen 2008; Lares et al. 2011), where redder satellite galaxies tend to have more concentrated profiles than blue satellites. Central galaxy properties are also important factors for the satellite profiles. Using SDSS DR8 data, Wang et al. (2014b) found that lower mass central galaxies have a steeper slope for the satellite radial distribution which is dominated by blue galaxies, while higher mass host galaxies have dominant component of red galaxies. However, Nierenberg et al. (2011, 2012) used statistical inference on galaxies in well-studied COSMOS field at $0.1 < z < 0.8$ and found that power-law slope of satellite radial distribution doesn't depend on host stellar mass or satellite luminosity. Although some agreements have been achieved on satellite distribution, detailed conclusions vary across studies partly due to the fact that vastly different datasets have been used and that sample selection methods in literature are not the same.

1.1.3 Environmental Effect in Simulation

The radial number density distribution of satellites has also been investigated within some simulations. For example, Sales et al. (2007) used data from the Millennium simulation (Springel et al. 2005) and found that the average profile can be well described by an NFW profile, which indicates that they trace dark matter very well. However, more recently, Brainerd (2018) calculated the typical profile from the Illustris (Vogelsberger et al. 2014) simulation and concluded that while at radii greater than $0.3r_{500}$ the satellites follow the dark matter distribution, they do not within that radius.

1.2 Motivation and Goal of this research

To investigate environmental effects, we chose to study the number density of satellites because they are good indicators of the galactic environment and our data has the ability to constrain their number density distribution. Along with environmental quenching and stripping, environmental effects can also determine the motion of the satellite galaxies within the dense environment. Therefore, the primary goal of this research is to study the radial number density distribution of satellite galaxies close to isolated massive galaxies which are likely to be central galaxies in cluster-like or group-like environments, and to study the evolution of the distribution. Eventually, we will discuss physical mechanisms that may play roles in shaping the number density distribution.

To systematically study the number density distribution of satellite galaxies, one needs a very large sample to suppress statistical concerns. The CFHT-CLAUDS (Sawicki et al. 2019) and Subaru-HSCSSP (Aihara et al. 2018) 18.6 deg^2 deep imaging data is deeper and/or wider than previous studies that discuss the same topic, it enabled us to push the study of the number density of satellite galaxies to lower stellar mass and higher redshift while keeping good statistical significance. We are able to study the number density of satellite galaxies at large range of stellar mass and redshift. We also split our sample to study the dependence of the number density distribution on stellar mass and star-formation activity.

The thesis is structured as follows: Chapter 2 describes the dataset and data reduction. Chapter 3 shows the methods used to measure the radial number density distribution for satellites. Chapter 4 shows the distribution for the whole sample as well as various subsamples. Chapter 5 shows discussion on some features of our results and compare with other studies. Chapter 6 shows our conclusions.

Chapter 2

Deep and Wide Imaging Data

2.1 The CLAUDS+HSC Survey

For the purpose of this study, a multi-wavelength survey is necessary, because many measurements rely on the wide wavelength coverage and some physical parameters to be derived from the multiwavelength dataset, such as redshift, stellar mass, star-formation probability. The larger the wavelength coverage, the better the determination of physical parameters. Moreover, a large area and deep depth is also required as we need large sample of galaxies for good statistics.

Therefore, we used imaging data from Hyper Supreme Camera (HSC-SSP s16a internal release) five-band (g, r, i, z, y) photometry (Aihara et al. 2018) on Subaru telescope, combined with CLAUDS (CFHT Large Area U-band Deep Survey, Sawicki et al. 2019) U-band

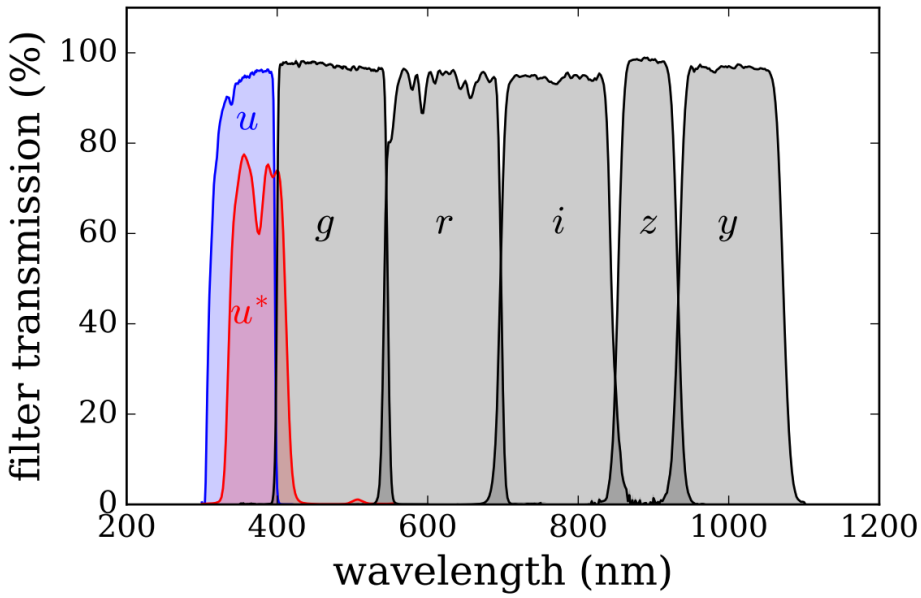

Figure 2.1: Filters avialable in CLAUDS and HSC-SSP surveys.

data, whose sky coverage matches the same regions as in HSC-SSP Deep layer. The wavelength coverage is illustrated in Figure 2.1. The area of both the surveys is ~ 18.6 deg^2 in the Deep layer, which includes four legacy fields: COSMOS, ELAIS, DEEP2, XMM-LSS. These two deep surveys are very deep and wide, thus we have a wide imaging data coverage from UV to optical (rest frame). The HSC data have a magnitude limit of $i_{\rm AB} = 26.8$ (5σ depth for point source) in the deep layer. CLAUDS also has an average U band depth of $U_{\rm AB} = 27$. The median seeing is about $0.92''$ (typically less than $1''$), which translates to about 7.5 kpc at $z = 1$.

2.1.1 Data Reduction

Data reduction was done as described in CLAUDS overview paper (Sawicki et al. 2019) and HSC-SSP overview paper (Aihara et al. 2018). Areas of bad photometry and contamination objects were masked out. Source detection was done by SExtractor. We then adopt the star-galaxy separation algorithm from Golob et al. (in prep). The algorithm uses XGboost which is an implementation of gradient-boosted-tree algorithm. It takes an object's colors, magnitudes and morphology information to classify an object. We made a cut in the catalog by the final prediction parameter `preds_median` at `preds_median<0.89` to choose galaxies.

Combined together the two very deep and wide surveys, our dataset has the unique advantage that it is extremely deep and meanwhile relatively wide. On the one hand, the relatively large area ensures that we can detect enough number of those rare massive galaxies to examine the population as best as we can. On the other hand, the depth of our data ensures that we are able to detect faint satellite galaxies around them. This unique feature made it possible for us to find more fainter satellite galaxies to perform better environment study around those massive galaxies.

2.1.2 Photometric Redshifts

Since getting spectra for every galaxy in our field ($\sim$ 5 million in total) would be impossible, we rely on photometric redshift to identify satellite galaxies and associate them to central

galaxies. Here we briefly introduce the method for estimation of photometric redshift in this paper (A.Golob, PhD thesis). We used a k-th nearest neighbor (kNN) method in a 5 dimensional photometric color space to estimate redshift. With a COSMOS 30 band training sample (Laigle et al. 2016) provided, redshift values were assigned to unknown objects by combining redshifts of nearby reference objects using a weighted kernel density estimation. Our photometric redshifts typically have scatter $\sigma_z = 0.044 \times (1+z)$ at $z < 1$ for faint objects, and also achieved good outlier rate and bias. Quality of redshift does not drop significantly for fainter objects, as validated by a close pair analysis (Huang et al. 2013).

In this study we restrict our analysis in the redshift range of $0.3 < z < 0.9$. We used this redshift range because below $z = 0.3$, outlier rate is higher than acceptable and above $z = 0.9$, quality of mass estimation drops due to our wavelength coverage. Our final sample includes $\sim 2,000,000$ galaxies in this redshift range.

2.1.3 Physical Parameters

Stellar masses were estimated in Golob et al. (in prep.). We estimate stellar mass through SED fitting using the template fitting code LePhare (Arnouts et al. 1999), comparing observed SEDs to a set of BC03 stellar population synthesis models (Bruzual & Charlot 2003) while assuming exponentially declining SFH, $0.008Z_\odot - 0.2Z_\odot$ metallicity, three dust attenuation laws (Prevot et al. 1984; Calzetti et al. 2000; Arnouts et al. 2013), various ages (0.1 - 30 Gyr), etc. Errors on stellar mass are defined as 68% confidence interval of the

marginalized posterior mass probability distribution.

For estimation of star-formation activity, we estimate probability of a galaxy being star-forming using a feature we call star formation probability (sfProb or $p_{\rm SF}$), ranging from 0 (quiescent) to 1 (star forming). sfProb were estimated using color-color diagrams in $u-r$, $r-y$ through a support vector machine (SVM) based probability assignment code. It is similar to the widely used UVJ diagram (e.g. Williams et al. 2009; Laigle et al. 2016) and trained on a sample of UVJ-classified galaxies in COSMOS, but modified due to the filters available to us (A.Golob, PhD thesis, see also Golob et al. in prep).

The distribution of these two parameters for satellite galaxies, background contamination objects and central galaxies is shown in Figure 2.2. In the upper panel of Figure 2.2 we show distribution of sfProb. Central galaxies are mostly quiescent. We did not observe a clear bimodality for satellite galaxies but only a mild peak at the quiescent end. This is mostly due to the fact that we used three nearby filters *ury* (with no infrared filters) to estimate star formation activity, resulting in relatively large uncertainty in star formation probability. In the lower panel of the same Figure we show mass distributions of the galaxies.

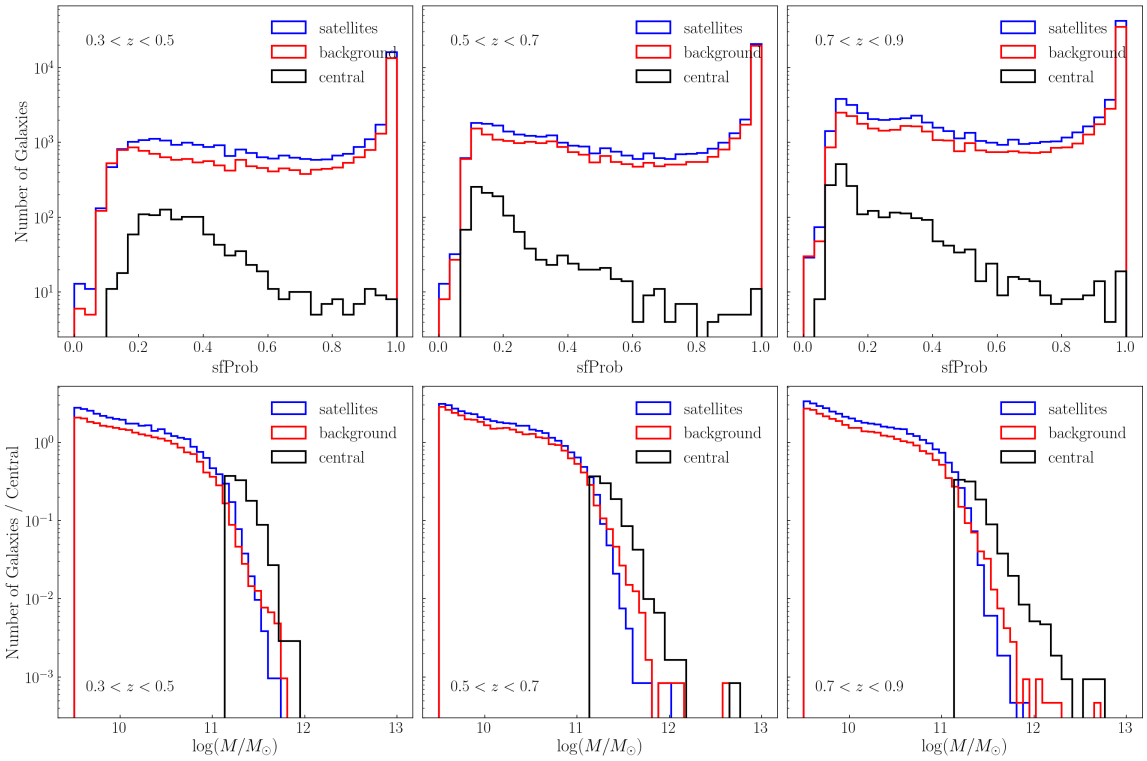

Figure 2.2: Star forming probability (sfProb) and stellar mass distribution of probable satellites in central apertures, background contamination sample in background apertures and central galaxy sample at $0.3 < z < 0.5, 0.5 < z < 0.7, 0.7 < z < 0.9$.

2.2 Sample Selection

2.2.1 Central galaxy sample

To study the satellite galaxy population in our dataset, we need to first define a central galaxy sample that host the satellite galaxies. Although we won't be able to individually confirm their central identity, most of them would sit in cluster-like or group-like environment. We select central galaxies first by their mass, including only $\log(M_{cen}/M_{\odot}) > 11.15$ galaxies in our catalog. This choice of mass cut is somewhat arbitrary, but it enables us to choose the most massive galaxies in our sample and ensure the field won't be too crowded for clean regions to estimate the background contamination level for the satellite sample. We then apply isolation criteria to ensure that the massive galaxies do not have a heavier companion within 700 kpc projeced radius and on the line-of-sight within redshift difference of $|z - z_{cen}| < 4.5 \times \sigma_z$, (where $\sigma_z = 0.044(1+z)$,three times the redshift selection interval for photometric surveys suggested in Malavasi et al. (2015)), so that we can assume them to be central galaxies in their own local environments. Our final sample of central galaxies (Table.2.1 shows number in each redshift bins we study) consist of 4294 massive galaxies that also meet isolation criteria across the redshift range $0.3 < z < 0.9$. The sample size is smaller than most low-redshift studies (e.g. $\sim$28000 in Tal et al. 2012a) but bigger than most high-redshift studies (e.g. $\sim$3400 in Nierenberg et al. 2012). We directly separate star-forming and quiescent central galaxies by making a cut at probability of

Table 2.1: Number Counts of Central and Satellite Galaxies with Redshift

Redshift (z)	N	N_{sf}	N_q	$\langle N_{sat} \rangle$	$\langle N_{sat,sf} \rangle$	$\langle N_{sat,q} \rangle$
$0.3 < z < 0.5$	1022	169	853	10.4	6.9	3.5
$0.5 < z < 0.7$	1193	123	1070	8.8	5.2	3.6
$0.7 < z < 0.9$	2219	204	1875	10.6	6.9	3.7

being star-forming `sfProb`$= 0.5$. We found that most of the centrals are quiescent. This is consistent with stellar mass function studies at similar redshift (e.g., Davidzon et al. 2017).

Figure2.4 to Figure2.8 show where our central galaxies and where we choose to make background estimations. In SXDS field (Figure 2.8), we removed the objects in the region where SXDS overlap with XMM-LSS field (Figure 2.7). Some background regions are located in regions where there is no observed objects due to issues in our random point catalogs (where we choose locations for background estimation), but since there are only a few of them and because distribution of background object number density is independent of location (see Figure A.1), this drawback will not affect our radial dependence study for satellite number density.

2.2.2 Satellite galaxy sample

After defining the central galaxy sample, we then constructed the potential satellite galaxy sample by selecting galaxies that are close to one of the central galaxies previously defined. We selected potential satellite galaxies in a cylinder centered on each central galaxies previously selected, selecting first by physical projected radius 700 kpc, then on the line-of-sight

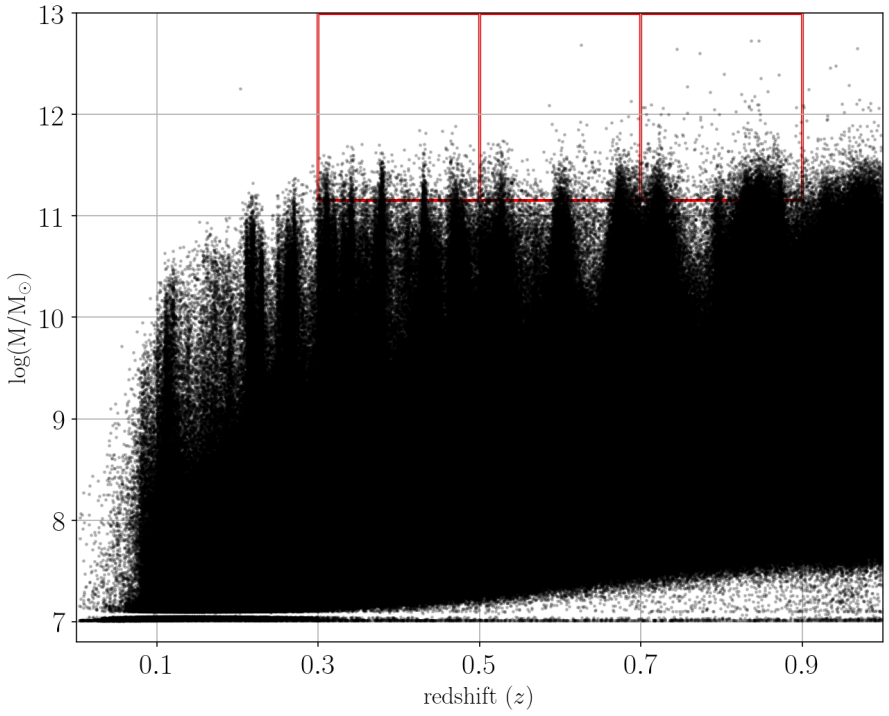

Figure 2.3: Stellar mass against redshift plot for all galaxies in our dataset. The three red boxes show our mass selection criteria for central galaxies in three redshift bins, minimum mass is set at $\log(M/M_\odot) > 11.15$. In total, 5547 central galaxies were selected.

select galaxies within redshift difference of $|z - z_{cen}| < 4.5 \times 0.044(1+z)$ from its nearby central. To ensure mass completeness in $0.3 < z < 0.9$, we put lower mass limits on satellite sample at $\log(M_{sat}/M_{\odot}) > 9.5$, and we keep this mass cut at all redshifts to be consistent. This lower satellite mass bound is roughly $\sim$2% of central galaxy mass, determined via simulated fake galaxies to give 85% completeness at all redshifts (Golob et al., in prep). An example of selected potential satellite galaxies around one central galaxy is shown in Figure 3.1.

As discussed in section 2.1.3, we quantify star formation activity by assigning each galaxy a probability of being star forming (`sfProb`) based on previously mentioned *ury* diagram. When counting numbers of star-forming and quiescent satellites, instead of classifying galaxies by making a direct cut in the parameter `sfProb` , we adopted the following statistical weighting method: if a galaxy has `sfProb==`a (where a range from 0 to 1), we count it as a star-forming galaxies and $1-a$ quiescent galaxies. This method makes our results suffer less from misclassification (Figure 2.2 shows that bimodality in star-formation activity that's supposed to exist is smeared out because of our limited wavelength coverage, but a dip in the middle is still visible). We found that most of the centrals are quiescent across the redshift range $0.3 < z < 0.9$.

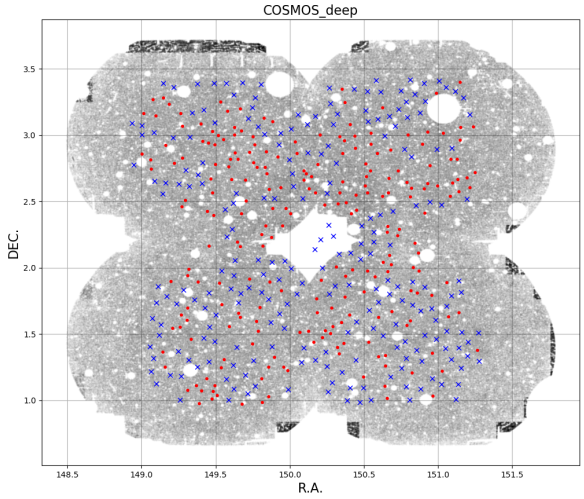

Figure 2.4: Sky-plot of Background Aperture Positions in COSMOS_deep Field using $0.3 < z < 0.5$ redshift bin. Blue crosses show the randomly placed background aperture positions. Red dots are positions of massive galaxies, including those that do not meet isolation criteria. Underlying gray dots show all the galaxies in this field.

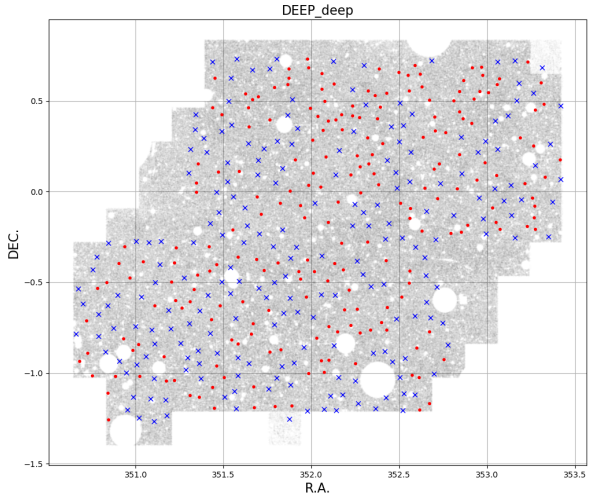

Figure 2.5: Sky-plot of Background Aperture Positions in DEEP_deep Field.

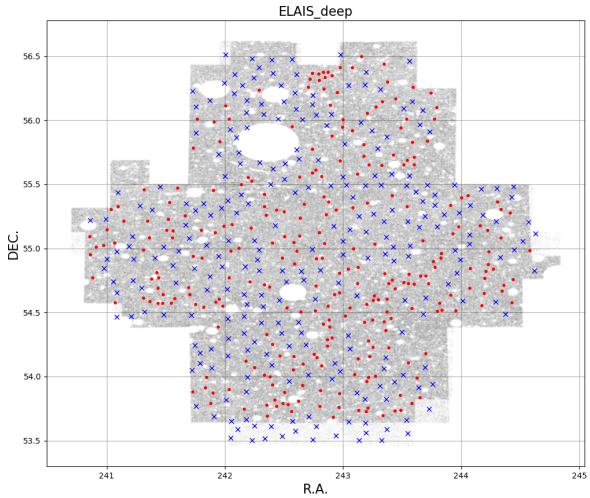

Figure 2.6: Sky-plot of Background Aperture Positions in `ELAIS_deep` Field.

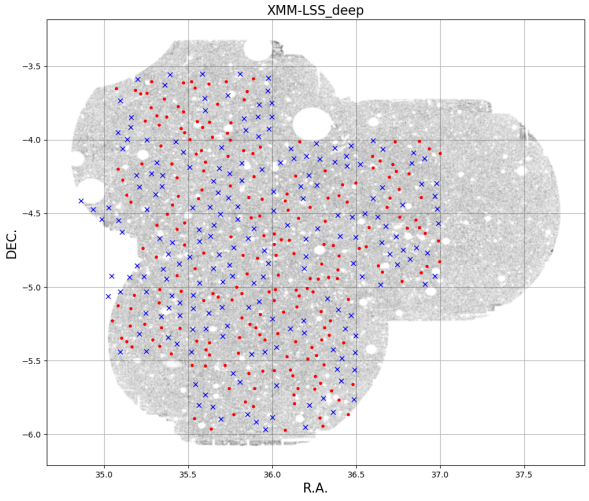

Figure 2.7: Sky-plot of Background Aperture Positions in `XMM-LSS_deep` Field.

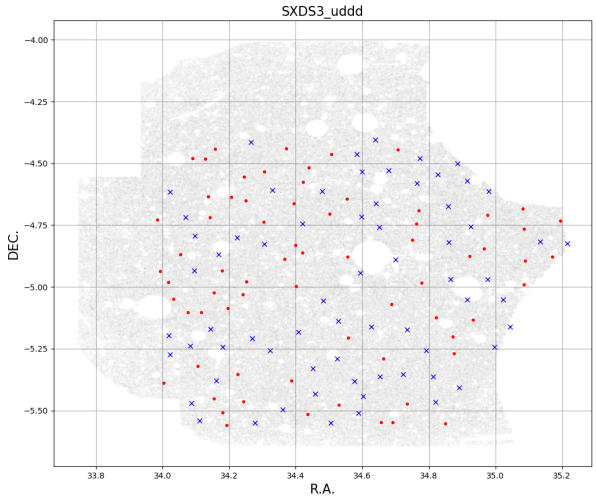

Figure 2.8: Sky-plot of Background Aperture Positions in SXDS_uddd Field.

Chapter 3

Satellite Spatial Distribution

3.1 Background Subtraction

Our potential satellite sample is complete but contaminated by foreground/background interlopers because our photometric redshift selection does not confirm association of satellites to centrals for individual satellites. We deal with this contamination via a statistical correction, using randomly positioned circular apertures with 700 kpc radius in the same field as we select the targeted central galaxies, similar to background subtraction method in Tal et al. (2012a). We repeat this procedure for each central galaxy. To be consistent with the satellite sample selection, we applied the same selection criteria we made for galaxies in circular apertures around central galaxies on the random apertures (i.e. same mass cut, projected radius range and redshift range cut). We additionally require that these background

apertures not overlap with apertures around central galaxies, and we also require they do not overlap each other to avoid possible selection bias because of multiple counts of the same objects. In some redshift bins, the field can be crowded with central galaxies, so we restrict ourselves to stop sampling background apertures when there is no space for extra background apertures. Right panel of Figure 3.1 is an example of selection of background contamination objects. Figure 2.4 to Figure 2.8 shows positions of our massive galaxies (including those that do not meet isolation criteria) and background apertures in all of our fields.

Typically, even after the photo-z cuts, the number of selected galaxies in random background apertures is as large as 60-70% of the number of selected galaxies in central galaxy apertures. That is to say, the signal of the satellite population is actually quite weak, so we need to stack our satellite population for each central galaxy to build up statistics for the number density of "true" satellites and be careful about estimating background level. The separation of star-forming and quiescent background galaxies were done in the same manner as for the satellites as described in Section 2.2.2. We stack both central aperture number counts and random aperture number counts (We tested background distribution in Appendix A and confirmed that it is reasonable), then subtract the two to statistically constrain the average number density of satellites for a sample of centrals.

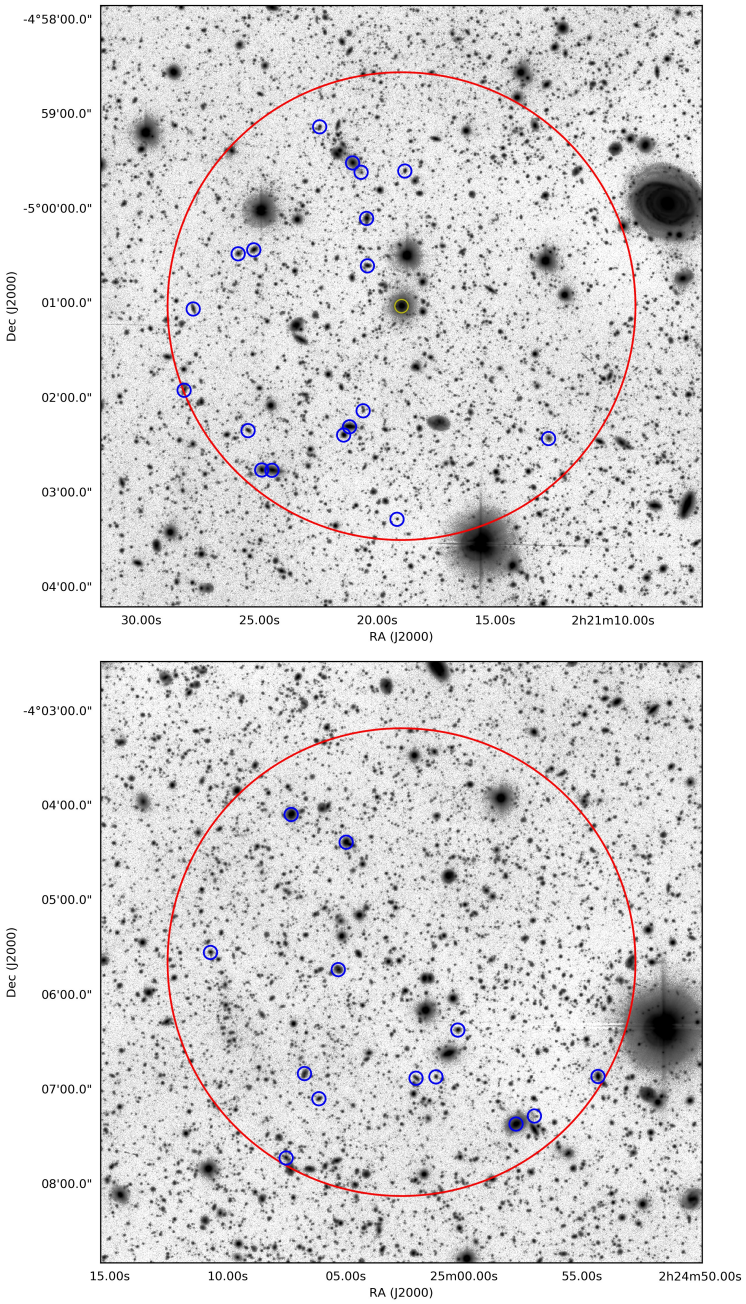

Figure 3.1: Example of probable satellite galaxy selection in central aperture (upper panel) and background aperture (lower panel). The big red circle shows 700 kpc radius satellite search region. Objects labelled by small blue circles are potential satellite galaxies (in central aperture) and contaminating objects (in background aperture).

3.2 Corrections

Due to inevitable limitations in our survey, some corrections for the number of detected satellites have to be made to correctly quantify satellite distribution. The main corrections we made are a correction due to masking in survey and a correction for incompleteness due to blending with the central galaxy.

3.2.1 Mask correction

Because of bright stars and bad photometry in some areas of the survey, some regions are masked from science analysis. Some apertures around central galaxies overlap with these masked regions, this would cause our satellite counts to drop if satellites happen to land in masked regions. In order not to bias the area of the aperture where we count satellites, we correct for these overlapping masked regions. We made use of the random point catalog (Golob et al. in prep.) to estimate how much correction we need. The random point catalog consists of uniformly distributed fake objects (only position information were set for the fake objects), following the same geometry as the real data.

We apply the same masking on objects in the random point catalog as we did in real objects, and use the ratio of number of random points before masking and after masking in each annulus as a proxy for the amount of correction we need on the sampling area. Using random catalogs, we count random points in the same apertures as for central galaxy and background subtraction, and calculate the masked rate of random points in those apertures,

and make corrections accordingly. In order to reduce variance due to low number counts in some annuli, we also stack random point counts in all apertures before we calculate the correction.

3.2.2 Spatial incompleteness correction

Since we are investigating the radial distribution of satellites, we need to pay attention to satellites that are within a few tens of kpc of the central galaxy, because they provide crucial information about how satellite galaxies behave in densest regions. However, detection of those galaxies may suffer from light pollution of central galaxy, thus having a lower completeness than objects at large radii. Therefore, for us to be confident about number density of satellites in the vicinity of central galaxy, it is necessary to do completeness estimation that is dependent not only on mass, but also on projected distance to the central galaxy.

We simulate model galaxies and place them close to central galaxies and find the recovery rate to estimate completeness. We did not directly generate model galaxies by manually providing parameters in certain models (e.g. Sersic) as is often done. Instead, we used the approach of Golob et al. and SExtractor's (Bertin & Arnouts 1996) `CHECKIMAGE` feature to generate Sersic models on detected real galaxies in a certain region and use them as mock galaxies. Then we add the `CHECKIMAGE` to the original image and re-detect around central galaxies to find the recovery rate. This process is repeated 10 times for the image of each

central galaxy environment to build up statistics. The advantage of this approach is that we already know physical information about these mock galaxies, and the population of mock galaxies have a similar distribution of properties as the real ones, which makes completeness estimation more realistic. The disadvantage is that we cannot control exactly where we put model galaxies, which we overcome by shifting positions for model galaxies in the same region.

We here provide completeness estimation against radius as several curves in Figure 3.2, along with their errors calculated by bootstrapping the model galaxy sample. We then can use these curves for corrections on the number density profiles. Completeness decreases with lower radius at all redshifts, showing that we do suffer contamination from central galaxies when detecting nearby satellites. However, for satellites in mass range $\log(M/M_{\odot}) > 9.5$, at radius greater than 50 kpc, detection completeness is close to the completeness level in the field and is kept constant out to 700 kpc.

3.3 Radial Number Density Distribution of Satellites

To calculate the number density of satellite galaxies at different projected distance to the centrals, we place circular annuli around selected massive central galaxies (i.e. we bin satellite galaxies in projected radius bins), count the number of satellite galaxies in each annulus with incompleteness corrections applied, and then divide these numbers by the mask-corrected area of each annulus to find the number density. We did not scale our

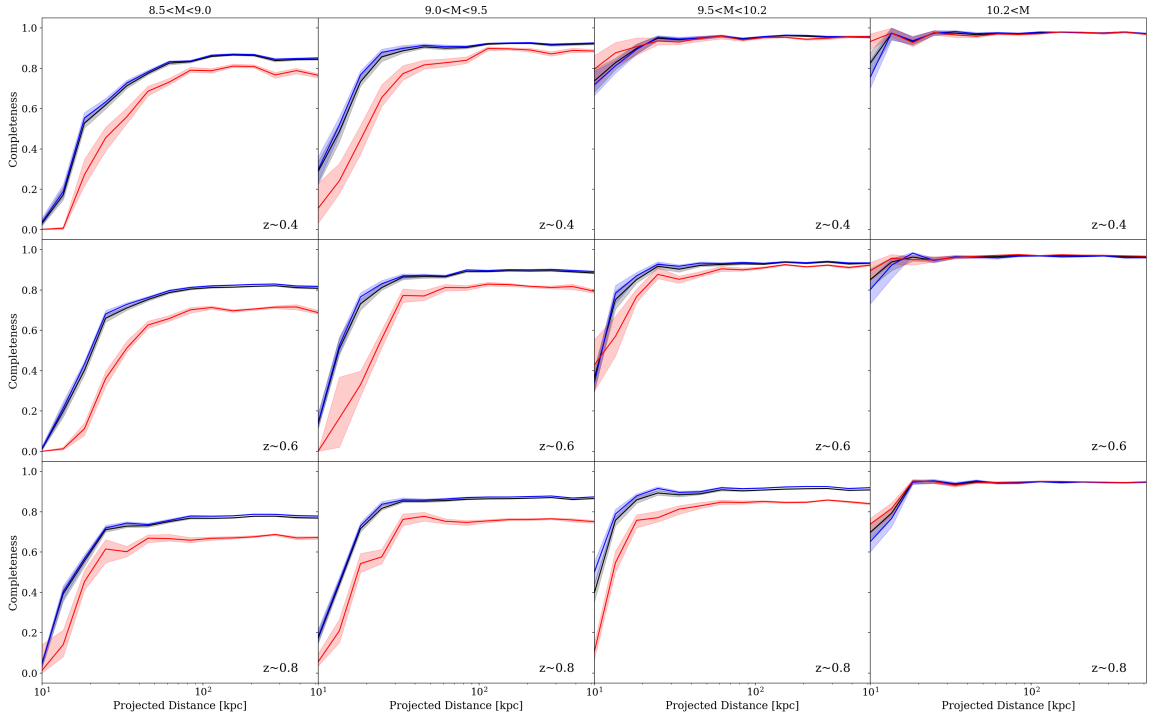

Figure 3.2: Spatial completeness curves. Black, red and blue lines are median completeness curves for total, quiescent and star-forming satellites respectively (using the separation in Section 2.2.2). Shaded region around each line shows the 16% to 84% bootstrap error.

number density profiles by r_{200} of the host halos the central galaxies are in, because scatter in observed stellar halo mass relation is still large (Leauthaud et al. 2012b; Coupon et al. 2015). To build up statistics, we stack satellite number density distributions around all the central galaxies and then normalize by the number of central galaxies to get an averaged radial number density distribution of satellites, which can be calculated as:

$$n_i = \frac{N_{sample,i} \cdot W_{comp,i} \cdot W_{mask,i}}{N_{central} \cdot A_i} - \frac{N_{bkg,i} W_{comp} \cdot W_{mask,i}}{N_{bkg} \cdot A_i}, \tag{3.3.1}$$

in which i represents i-th radial bin, $N_{sample,i}$ and $N_{bkg,i}$ are the number of objects in the central galaxy apertures and associated background apertures. W_{comp}, W_{mask} are the weights for distance-dependent spatial incompleteness and masking (i.e. area correction) we apply on the number counts, which we described in Section 3.2. Although we cannot confirm association for any individual potential satellite with its central galaxy, by stacking hundreds of central galaxies with statistical corrections we can build a satellite galaxy sample that mostly reflects the cluster or group environment.

3.3.1 Model Fitting Approach

Following the common choices in the literature, we will fit the radial satellite number density distribution (surface number density against projected radius toward central galaxy) with the following profiles:

1) The power law profile:

$$\Sigma(r) = r^{-\gamma} \tag{3.3.2}$$

where Σ is the number density, r is the distance to central galaxy and γ is the power index. The power law profile does not have any physical motivation but quantifies the slope of distribution.

2) The original NFW profile (Navarro et al. 1995):

$$\rho(r) = \frac{\rho_0}{\frac{r}{r_s}\left(1+\frac{r}{r_s}\right)^2}, \tag{3.3.3}$$

where r_s is a characteristic radius of the profile and ρ_0 is the normalization parameter. The NFW profile is usually used to describe dark matter distribution in dark matter halos.

The projected NFW profile was derived from the original one to work with projected surface density profiles (Bartelmann 1996):

$$\Sigma(x) \propto \begin{cases} \left(x^2-1\right)^{-1}\left(1-\frac{2}{\sqrt{x^2-1}}\arctan\sqrt{\frac{x-1}{x+1}}\right) & (x>1) \\ 1/3 & (x=1) \\ \left(x^2-1\right)^{-1}\left(1-\frac{2}{\sqrt{1-x^2}}\operatorname{arctanh}\sqrt{\frac{1-x}{1+x}}\right) & (x<1) \end{cases}, \tag{3.3.4}$$

where $x \equiv r/r_s$.

3) Sérsic profile (Sérsic 1963):

$$I(R) = I_e \exp\left\{-b_n\left[\left(\frac{R}{R_e}\right)^{1/n} - 1\right]\right\}, \tag{3.3.5}$$

where I_e is the normalization factor, r_e is the effective radius, n is the Sérsic index which controls the general shape of the distribution and $b_n = 2n - 1/3$. The Sérsic profile is usually used to describe light distribution in galaxies.

The model-fitting tool throughout this study is `scipy.optimize.curve_fit`, a least square fitting method from SciPy (a python scientific computation package). We quantify goodness of fit by the χ^2 statistic per degree of freedom,

$$\chi^2_{dof} = \frac{1}{\nu}\sum_i \left(\frac{f_i - n_i}{\sigma_i}\right)^2, \tag{3.3.6}$$

where n_i is the number density of satellites in one bin, σ_i is the associated errobar and f_i is the value of fit function at that point. ν is degree of freedom and is defined as number of data points minus number of parameters. Uncertainties of parameters are given by the algorithm and they are 1σ errors. We tried three fitting models: power law, NFW and NFW+Sersic.

Chapter 4

Results

In this Chapter, we present our results on the number density of satellite galaxies. With deep data and large samples at relatively high redshift ($0.3 < z < 0.9$), we can not only study the number density profiles of the total satellite sample, but also work on specific subsamples to investigate how the number density of satellites depends on certain physical parameters, which is helpful for interpreting the evolution of satellite population in dense environments. To ensure detection completeness, we only included satellites that have stellar mass $\log(M_{sat}/M_{\odot}) > 9.5$ for the whole satellite sample, for which mass range we are more than 85% complete at our highest redshift $z = 0.9$ (determined through simulated fake galaxies in Golob et al. in prep), and for which incompleteness corrections are therefore fairly minor.

We use satellites whose projected distance to its central galaxy are between 10kpc and

700kpc (projected distance measured at central galaxy's redshift and assumed WMAP9 cosmology) to quantify the radial number density profile. We choose these boundaries because within 10kpc, the light from central galaxy dominates so we cannot confidently detect satellites within this radius (as shown in completeness curve in figure.3.2, completeness at 10kpc is already very low), and beyond 700 kpc, the satellite population is not significant, and the number density is almost at field level. Between these two boundaries, we make bin sizes that increase exponentially with radius. When plotting, we average the radii of all galaxies in one bin and plot each data point at that averaged radius to reduce the bias in radius binning. This exponential binning scheme also gives us a more detailed look at the inner regions of massive galaxy environment.

First, in Section 4.1, we show the radial number density profiles of total satellite galaxy sample with star-forming activity dependence, and we quantify redshift evolution in Section 4.3. Then we examine the various dependencies of the radial satellite number density distribution in Section 4.2

4.1 Total Satellite Sample

We first present in Figure 4.1 the radial number density of satellites for the whole sample in the redshift range $0.3 < z < 0.9$. A satellite population is clearly detected around our central galaxies and a clear radial distribution is present where the number density of satellites decreases with increasing projected distance from central galaxy. We then separate the

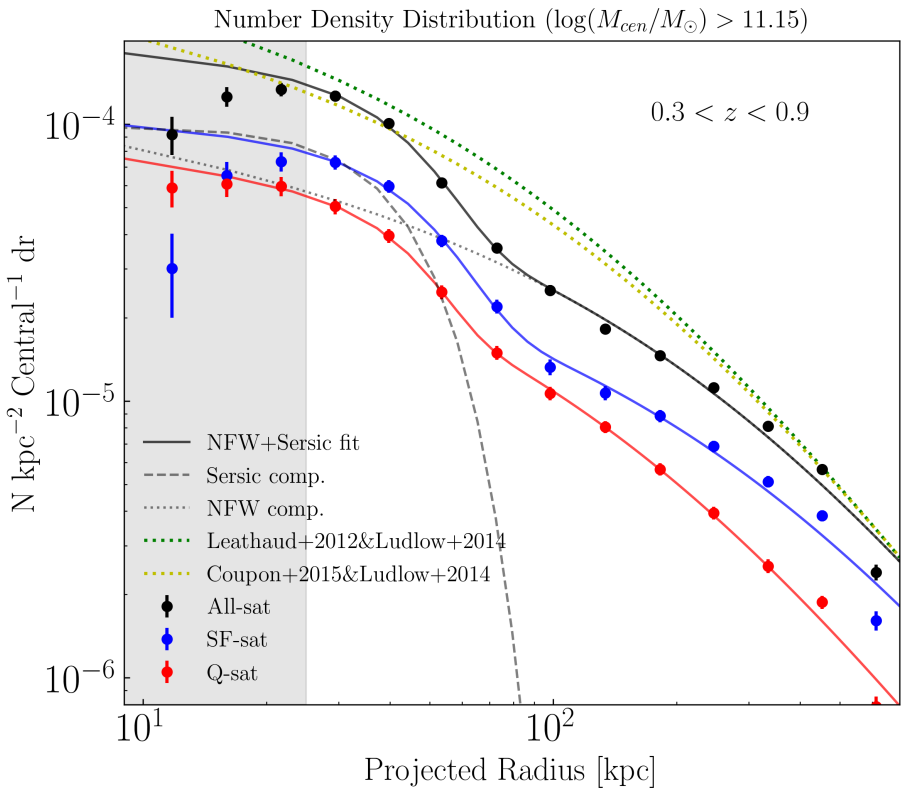

Figure 4.1: Radial Number Density of Satellites in $0.3 < z < 0.9$. The centrals are cut for mass higher than $10^{11.15} M_\odot$ and the satellites are cut for mass higher than $10^{9.5} M_\odot$. Grey shaded region shows where our data become incomplete and thus excluded from model fitting. Black, red and blue dots with Poissonian errorbars show total, quiescent and star-forming satellite profiles. In each panel, the solid line shows our best fit Sersic+NFW model, with the two component labeled by dashed and dotted line. The dark matter mass density profile predictions (yellow and green dotted lines) are generated using data from Coupon et al. (2015) , Leauthaud et al. (2012a) and Ludlow et al. (2014) which are then normalized to match number density of satellites fit in the outskirts with arbitrary unit.

satellite sample into star-forming and quiescent in each redshift bin by weighting each satellite by `sfProb` value as described before (section 2.1.3) and then measure the number density for the two subsamples, as shown by blue and red points in fig.4.1. The quiescent satellite galaxies have a higher concentration than the star-forming satellites, as the r_s value in NFW fit gives 179 ± 27 and 385 ± 95 for the two subsample respectively.

The next step is obviously to ask how do we model the distribution. Early papers fit a power law to the satellite radial number density distribution (e.g. van den Bosch et al. 2005; Chen 2008), which is consistent with the early noisy data. Thanks to improvements in sample size and growing depth of photometry, recent papers have shown that number density profile of satellites deviate from a simple power law distribution, and can instead be described by the NFW profile. The physical motivation of this choice of model is that satellite galaxies should follow dark matter subhalo number density distribution, which follows the NFW profile usually used for dark matter mass density distribution in the parent halo (Ludlow et al. 2009). However, several papers at low redshift using SDSS data (Tal et al. 2012a; Watson et al. 2012; Piscionere et al. 2015) found additionally that close to the central galaxies, there is a deviation of the satellite number density from the NFW prediction.

We fit power-law, NFW and Sersic+NFW models to the measured number density profiles (Figure 4.1). We choose not to fit the three innermost data points (within 25 kpc of the central position) because detection of satellites are severely incomplete due to contamina-

tion and deblending from central galaxy light there and would require heavy incompleteness corrections. The fit of distribution clearly deviates from a power law shape. With a NFW model fitting, there is still some deviation of satellites at small radii. Therefore, we choose to use the projected NFW model (derived from NFW profile in Bartelmann 1996) to fit our data at large radii and additionally use Sersic model to fit at small radii, following Tal et al. (2012a). This additional (deviation-from-NFW) feature on small scales is consistent with result from Tal et al. (2012a) at $0.04 < z < 0.2$ and Piscionere et al. (2015) at $0.02 < z < 0.165$, and we are the first to observe this deviation at $z > 0.2$. Specifically, the $\chi^2_{\rm dof}$ value reduces significantly from the power law model (2 parameters, $\chi^2_{\rm dof} = 39.98$) and NFW model (2 parameters, $\chi^2_{\rm dof} = 31.93$) to that of the NFW+Serisc model (5 parameters, $\chi^2_{\rm dof} = 1.96$), indicating that the model with Sersic+NFW components best describes the number density profiles.

To probe whether the satellite distribution resembles the underlying dark matter distribution, estimation of the dark matter distribution from the NFW model is overplotted in dotted lines. We first converted our central stellar mass to halo mass using stellar-to-halo mass ratio (SHMR) from either Equation.15 and Table.5 from Leauthaud et al. (2012a) (green line) or Table.4 from Coupon et al. (2015) (yellow line), which were empirical relations derived using observations. We found that the halos where our central galaxies reside in have a median mass about $\sim 10^{13.6} M_{\odot}$(yellow) or $\sim 10^{13.3} M_{\odot}$(green). Then we calculated size of the dark matter halo r_{200} for each central galaxy using $r_{200} = (3M_{200}/(800\pi\bar{\rho}))^{1/3}$

where $\bar{\rho}$ is the critical density in the Universe and M_{200} is halo mass which include regions that have 200 times critical density in the Universe. We use r_{200} - concentration (c) relation in Figure 1 in Ludlow et al. (2014) to read off corresponding c value for our r_{200} estimates. Finally, we use the equation $r_s = r_{200}/c$ to convert r_{200} to r_s in the NFW model, we can then take median value of r_s and overplot the predicted NFW profile in Figure 4.1 with an arbitrary normalization scaled to the out-most data point. The estimated mass distribution for dark matter is more concentrated than our number density distribution for satellite galaxies. For the dark matter halos to have similar concentration as the satellites we observed now, the halo mass needs to be around $\sim 10^{14.1} M_{\odot}$ (using SHMR from Coupon et al. 2015).

Although the deviation from the NFW profile on small scale is significant, there is no clear physical explanation yet in the literature about how this two-component profile came into place. We can exclude that the deviation is due to the one-halo term (clustering signal due to galaxies clustered within the same halo) in galaxy clustering, because even the one-halo term has much larger scale ($\sim$ 1Mpc, e.g. Zehavi et al. 2004). We will investigate how this feature depends on physical parameters of centrals and satellites in the next subsections and give a tentative explanation in the discussion section.

4.2 Dependence on Various Properties

4.2.1 Central mass dependence

To study whether the radial number density profile of satellites is dependent on the mass of the central galaxy, we expand our massive central sample by extending the mass range down to $\log(M_{cen}/M_{\odot}) = 10.8$, and split the central sample into three mass bins ($10.8 < \log(M_{cen}/M_{\odot}) < 11.0$, $11.0 < \log(M_{cen}/M_{\odot}) < 11.3$, $\log(M_{cen}/M_{\odot}) > 11.3$), while keeping the same isolation criteria. Then we measure the number density distribution of satellites for each mass subsample of central galaxy.

In Figure 4.2, we show central galaxy mass dependence for our satellite number density distribution. We used $1.5\sigma_z$ redshift cut for isolation criteria and selection of potential satellteis/backgronud objects in this case to reduce errorbars. In the three panels, from left to right with increasing central masses, the slopes of each number density profile are consistent with no significant difference across all three central mass bins. But clearly more massive central galaxies have more satellites in the same halo, indicating the dark matter halo for the group/cluster is also more massive (Kawinwanichakij et al. 2014). Figure 4.2 also shows that quiescent fraction of satellites is dependent on central galaxy mass, as there are more quiescent satellite galaxies compared to star-forming ones around most massive central galaxies.

Central galaxy mass dependence has been investigated by many other studies, but con-

clusions are divided. For example, Kawinwanichakij et al. (2014) showed that more massive central galaxies host more satellite galaxies at mass ranges $10.48 < \log(M_{cen}/M_{\odot}) < 10.78$ and $10.78 < \log(M_{cen}/M_{\odot})$ at $1 < z < 3$.Nierenberg et al. (2012) found that satellite radial number density has no dependence on the host mass in mass range ($\log(M_{cen}/M_{\odot}) > 10.5$) in their intermediate-redshift ($0.1 < z < 0.8$) fitting power law profiles to the r_{vir}-scaled distribution. However, Prescott et al. (2011) found a shallower slope of radial number density profile for higher mass central galaxy at $0.01 < z < 0.15$, which indicates satellite galaxies follow dark matter halo as they live in more extended dark matter halos. Wang et al. (2014b) fit power law profiles to their SDSS DR8 r_{vir}-scaled satellite distribution but found such a dependence where slope of number density profile is shallower for higher mass centrals.

The differences among studies are partly due to the different mass range being used, as a large enough mass range may be necessary to observe a dependence of slope on central stellar mass. We did not observe such dependence using a relatively small mass range (~ 0.5 dex).

4.2.2 Central star-formation dependence

Galactic conformity as a systematic effect was first discovered in Weinmann et al. (2006) at $0.01 < z < 0.2$ and later discussed broadly in the literature both in intermediate redshift ($z < 1$, e.g. Kauffmann et al. 2013; Hartley et al. 2015; Hearin et al. 2016) and high redshift ($z >$

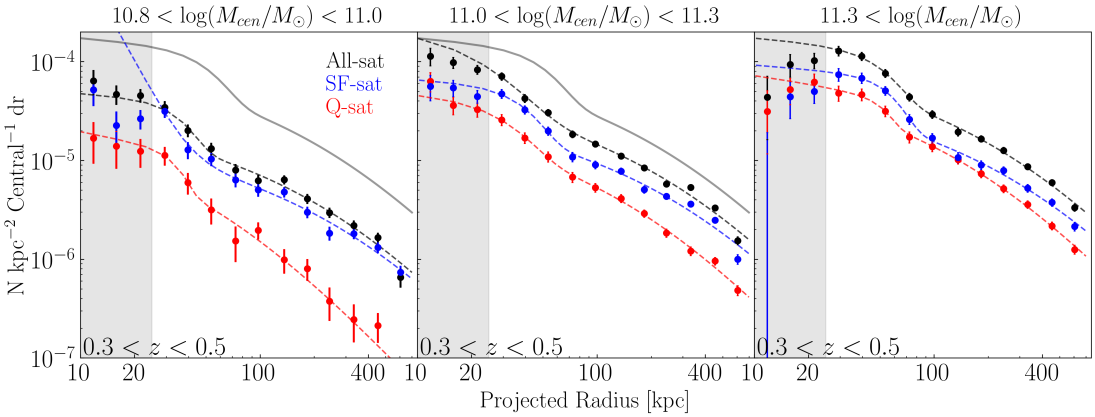

Figure 4.2: Satellite radial number density profile with different central galaxy mass dependence. Central galaxy mass range from left to right are:$10.8 < \log(M_{cen}/M_\odot) < 11.0$, $11.0 < \log(M_{cen}/M_\odot) < 11.3$, $\log(M_{cen}/M_\odot) > 11.3$. In each panel, black, red and blue dots represent number density of total, star-forming and quiescent satellites respectively. Shaded region show spatial incompleteness regions. The best fit curve for high mass central sample is plotted in all three panels for comparison.

1, e.g. Hartley et al. 2015; Hatfield & Jarvis 2016; Hearin et al. 2016). Galactic conformity states that there is a higher fraction of red satellite galaxies near red central galaxies than the fraction of red satellites around star-forming central galaxies. In this section we study galactic conformity by splitting our central galaxy sample into star-forming and quiescent subsamples by making a cut at `sfProb==0.5`, with the intention to study the physical scale and redshift dependence of galaxy conformity. Throughout our redshift range, there are significantly more quiescent centrals than star-forming ones.

In Figure 4.3 , we plot the radial number density distributions separately for satellites around star-forming centrals and quiescent centrals in $0.3 < z < 0.9$. We further split the central and satellite samples into three redshift bins (fig.4.4 to Figure 4.6), and found that quiescent fraction of satellites is higher around quiescent central galaxies at all three red-

shifts, indicating galaxy conformity was already in place at $z \sim 0.9$. Another feature in Figure 4.3 is that quiescent centrals have 30-40% more satellites than star-forming centrals. Such excess was also found in Kawinwanichakij et al. (2014) and in Guo et al. (2012). Moreover, satellite quiescent fraction around star-forming centrals is close to the quiescent fraction for field galaxies at the same redshift (shown in green horizontal line). In satellite sample around quiescent centrals, we observed quiescent fraction increases slowly toward the central galaxy, while around star-forming centrals, this trend is not significant. Our star-forming central galaxies have lower median stellar mass, and to rule out this mass selection bias, we constructed a stellar-mass-distribution-matched sample by down-sampling quiescent central sample and after the repeated analysis, we found the trends are still present (bottom panel of Figure 4.3).

4.2.3 Satellite mass dependence

We split our satellite galaxy sample into two stellar mass bins ($9.5 < \log(M_{sat}/M_{\odot}) < 10.2$, $10.2 < \log(M_{sat}/M_{\odot}) < M_{cen}$) and remeasured satellite number density distributions in these two bins respectively, using a wide single redshift bin $0.3 < z < 0.9$ (Figure 4.7). We then again performed NFW+Sersic model fitting for the two mass-split subsamples. We found that the Sersic component is more significant in low mass satellites, i.e. the two-component shape is more visible for low mass satellites. We relate this feature to mass dependence of tidal stripping and dynamical friction (Chapter 5).

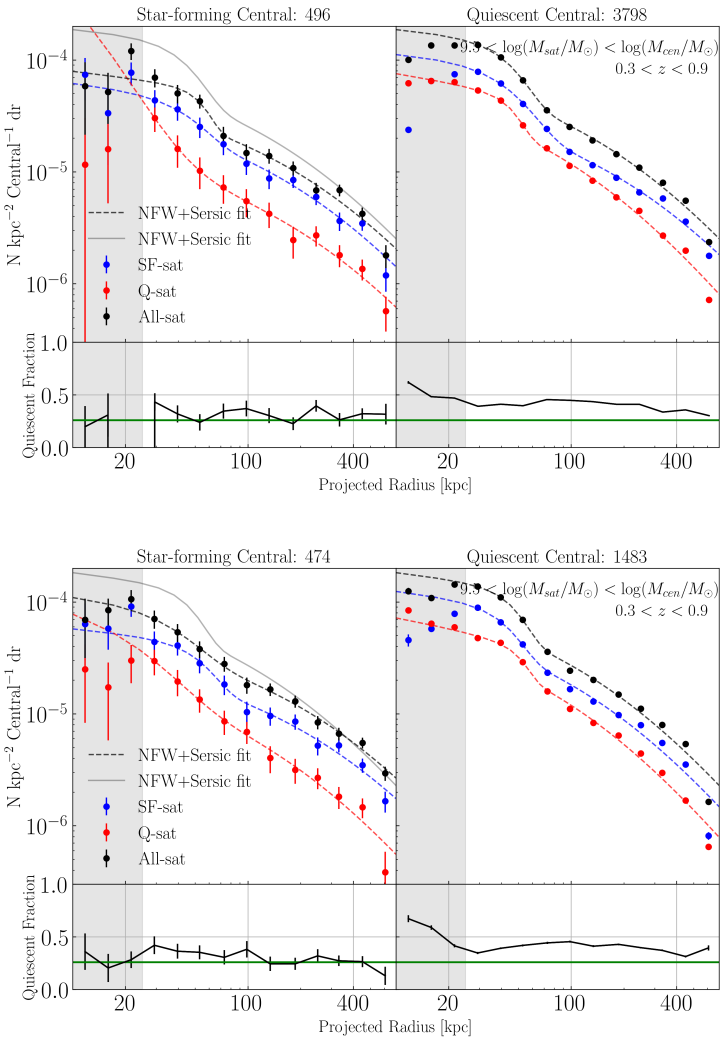

Figure 4.3: The top panels show the satellite radial number density profiles with central sfProb dependence, splitting by central galaxy star formation probability $0 <$ sfProb < 0.5 in left panel and $0.5 <$ sfProb < 1 in right panel. We used a large redshift range $0.3 < z < 0.9$ in this case. We also show quiescent fraction of satellite sample as a function of radius, and the green horizontal line represents quiescent fraction for field galaxies. For comparison, we plot total satellite sample fit curve for quiescent centrals also in the star-forming central panel. The bottom panels are the same as the top panels, but now the quiescent and star-forming centrals are matched in mass distribution.

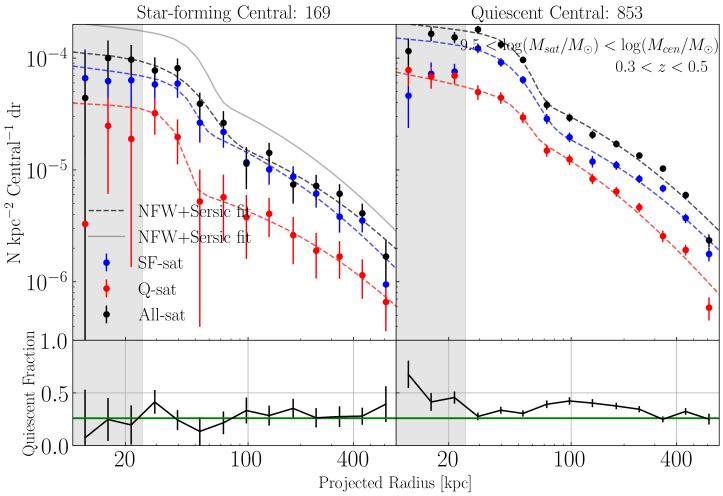

Figure 4.4: Satellite radial number density profiles with central sfProb dependence in $0.3 < z < 0.5$ bin, splitting by central galaxy star formation probability $0 <$ sfProb < 0.5 in left panel and $0.5 <$ sfProb < 1 in right panel. We also show quiescent fraction of satellite sample as a function of radius, and the green horizontal line represents quiescent fraction for field galaxies.

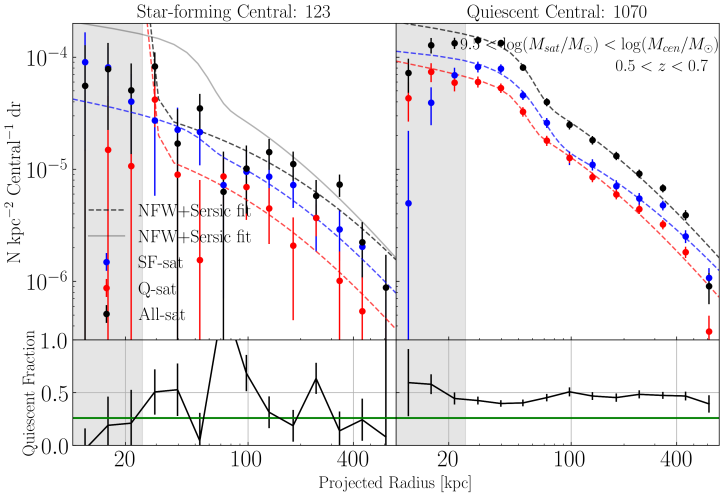

Figure 4.5: Satellite radial number density profiles with central sfProb dependence in $0.5 < z < 0.7$ bin, splitting by central galaxy star formation probability $0 <$ sfProb < 0.5 in left panel and $0.5 <$ sfProb < 1 in right panel. We also show quiescent fraction of satellite sample as a function of radius, and the green horizontal line represents quiescent fraction for field galaxies.

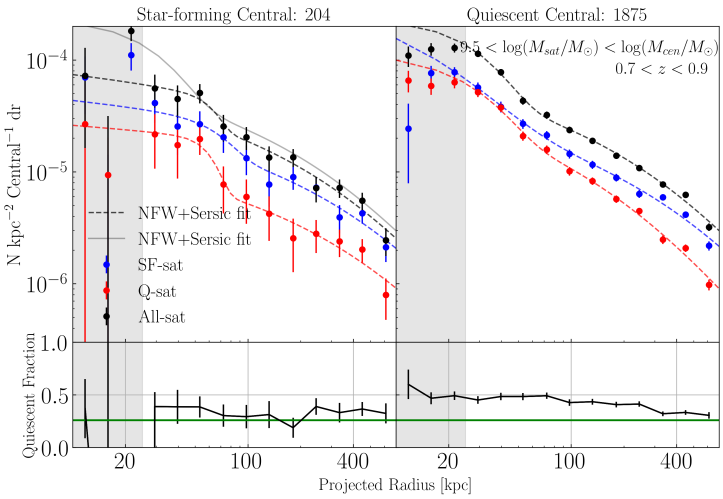

Figure 4.6: Satellite radial number density profiles with central sfProb dependence in $0.7 < z < 0.9$ bin, splitting by central galaxy star formation probability $0 <$ sfProb < 0.5 in left panel and $0.5 <$ sfProb < 1 in right panel. We also show quiescent fraction of satellite sample as a function of radius, and the green horizontal line represents quiescent fraction for field galaxies.

Table 4.1 shows characteristic radius r_s of NFW component in best-fitting models for mass and star formation-split satellite subsamples. Considering the whole redshift range (fig.4.7), satellites in the two mass bins have consistent r_s's, which means on large scale, they are comparable in terms of concentration. In both mass bins, characteristic radii (r_s) of NFW component of quiescent satellites are smaller than those of star-forming satellites, indicating that quiescent satellites are more concentrated at same mass. It is also worth noting that star forming satellites are more abundant than quiescent satellites in low mass bin but not in high mass bin.

Further split up in three redshift bins, r_s parameters of NFW model in all three redshift bins are also shown in Table.4.1. We found that concentration for low mass satellites is

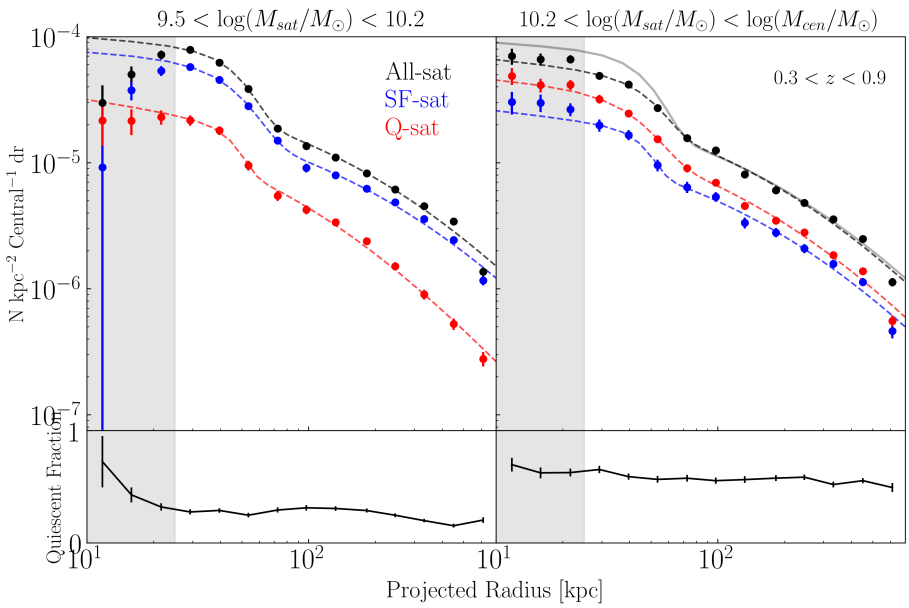

Figure 4.7: Satellite radial number density profiles for two mass bins. The satellite sample was split by satellite mass range $9.0 < \log(M_{sat}/M_\odot) < 10.2$ in left panel and $10.2 < \log(M_{sat}/M_\odot)$ in right panel. We used a large redshift range $0.3 < z < 0.9$ in this case. Black, red blue and red shows distribution for all, star-forming and quiescent satellite population respectively. Best fit Sersic+NFW models are shown in in dashed curves, the best fit curve for low-mass satellites is also plot in the high-mass satellite panel for comparison.

slightly higher in lower two redshift bins, but with r_s still consistent within errorbars. In summary, we did not observe mass segregation in $0.3 < z < 0.9$ redshift bins around our selected central galaxies.

In a similar satellite mass range with us, Hartley et al. (2015) found systematically steeper power-law slopes for massive satellite ($10.1 < \log(M_{sat}/M_{\odot}) < 10.5$) profiles than those of lower mass ones ($9.7 < \log(M_{sat}/M_{\odot}) > 10.1$) at $0.4 < z < 1.3$. At higher satellite mass range, Nierenberg et al. (2012) found no dependence of power-law slope on satellite luminosity on those with $\log(M_{sat}/M_{\odot}) > 10.5$ at $0.1 < z < 0.8$. Fitting with NFW profile, Guo et al. (2012) found that concentration of the profile decreases systematically with increasing satellite luminosity for satellites brighter than $m_r = 20.5$ in SDSS data. The inconsistency among studies may be due to the inhomogeneity of the datasets, as sample selection and parameter ranges are very different.

4.3 Redshift Evolution

We then measured radial number density distributions for the total satellite sample in three redshift bins $0.3 < z < 0.5, 0.5 < z < 0.7, 0.7 < z < 0.9$, keeping a constant mass cut for the selection of central galaxies at $\log(M_{cen}/M_{\odot}) = 11.15$ for the three redshift bins.

We detected 10.7, 8.7, 10.6 satellites for each central, on average, in the three redshift bins after accounting for background contamination. Figure.4.8 shows the background subtracted radial satellite number density distribution in the three redshift bins. The same fit-

Table 4.1: Characteristic NFW radius of best-fit Sersic+NFW profiles in mass-split satellite population. Q-Frac stands for quiescent fraction in low/high mass satellite subsample.

r_s (kpc)	Redshift	Q-Frac (L/H)	Low Mass Sat.	High Mass Sat.
total	$0.3 < z < 0.5$	0.23/0.45	226±62	283±71
star-forming	$0.3 < z < 0.5$		218±119	283±70
quiescent	$0.3 < z < 0.5$		115±31	225±55
total	$0.5 < z < 0.7$	0.30/0.59	173±59	236±57
star-forming	$0.5 < z < 0.7$		184±72	169±50
quiescent	$0.5 < z < 0.7$		145±24	219±66
total	$0.7 < z < 0.9$	0.19/0.58	501±99	356±119
star-forming	$0.7 < z < 0.9$		627±135	362±88
quiescent	$0.7 < z < 0.9$		179±36	289±89
total	$0.3 < z < 0.9$	0.23/0.55	304±65	274±52
star-forming	$0.3 < z < 0.9$		353±66	278±56
quiescent	$0.3 < z < 0.9$		137±20	243±53

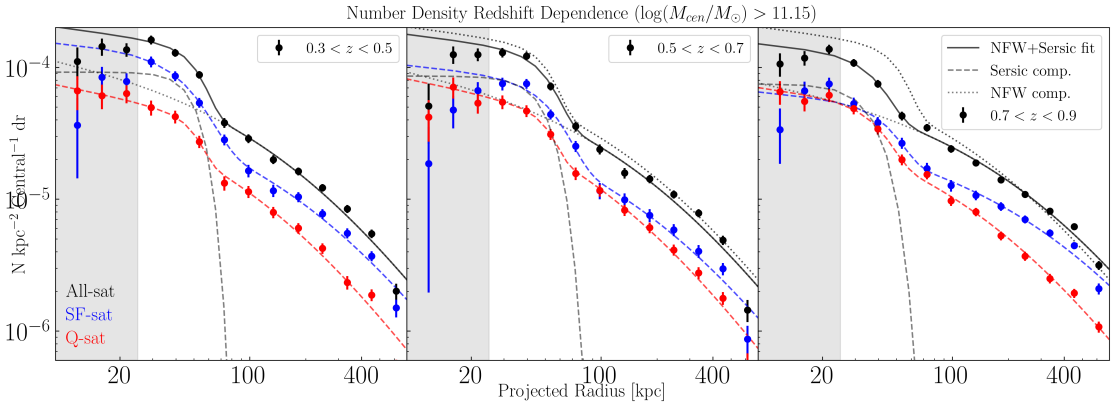

Figure 4.8: Radial Number density profiles in three redshift bins $0.3 < z < 0.5, 0.5 < z < 0.7, 0.7 < z < 0.9$. Grey shaded region shows where our data become incomplete, thus excluded from model fitting. Black, red and blue dots with Poissonian errorbars show total, quiescent and star-forming satellite profiles. In each panel, the solid line shows our best fit Sersic+NFW model, with the two component labeled by dashed and dotted line. $\chi^2_{\rm dof}$ value of each fit is indicated in the left bottom corner in each panel. For comparison, we also plot fitting curve from left panel in the other two panels (dotted line).

Table 4.2: Best fitting parameters of NFW+Sersic profiles for satellite population in three redshift bins. Profiles were fitted for total, quiescent and star-forming satellites respectively around the whole central galaxy sample.

Redshift	**Mass Range** [$\log(M/M_\odot)$]		**SF/Q Status**[1]		**Best Fitting Parameters**[2]					$\chi^2_{\rm dof}$
	Central	Satellite	Cen.	Sat.	r_s [kpc]	δ [$\times 10^{-5}$]	I_e [$\times 10^{-5}$]	r_e [kpc]	n	
0.3 - 0.5	11.15 - 13.0	9.5 - M_{cen}	all	all	219±55	3.83±1.17	8.73±1.98	31±24	0.19±0.17	3.90
0.5 - 0.7	11.15 - 13.0	9.5 - M_{cen}	all	all	231±82	3.13±1.34	7.2±2.22	34±9	0.23±0.21	6.35
0.7 - 0.9	11.15 - 13.0	9.5 - M_{cen}	all	all	346±48	2.27±0.33	6.20±1.77	27±3	0.26±0.20	2.44
0.3 - 0.5	11.15 - 13.0	9.5 - M_{cen}	all	sf	283±74	1.81±0.56	6.18±1.29	36±4	0.39±0.23	2.31
0.3 - 0.5	11.15 - 13.0	9.5 - M_{cen}	all	q	152±49	2.09±0.90	2.08±1.07	11±14130	0.17±0.26	3.21
0.5 - 0.7	11.15 - 13.0	9.5 - M_{cen}	all	sf	260±99	1.50±0.68	4.32±0.99	39±4	0.31±0.21	2.93
0.5 - 0.7	11.15 - 13.0	9.5 - M_{cen}	all	q	143±39	2.36±0.87	2.31±0.87	11±7096	0.17±0.12	2.00
0.7 - 0.9	11.15 - 13.0	9.5 - M_{cen}	all	sf	535±114	0.93±0.18	2.47±0.83	32±7	0.26±0.36	2.62
0.7 - 0.9	11.15 - 13.0	9.5 - M_{cen}	all	q	215±28	1.39±0.22	2.51±0.71	28±3	0.26±0.21	1.24

[1] sf=sfProb>0.5 sample, q=sfProb<0.5 sample, all=total sample

[2] Fitting parameters. r_s: characteristic radius of NFW component, δ: normalization for NFW component, I_e: normalization for Sersic, r_e: effective radius of Sersic component, and n: Sersic index.

ting procedure was followed for three distributions separately, parameters and goodness of fits are given in table 4.2. The fact that some estimate on effective radius of the Sersic component is not good indicates that Sersic profile may be not be best to destribe the deviation-from-NFW feature on small scales. Concerning the NFW component on large scale, we found that the characteristic radius r_s is consistent in the lower two redshift bins but is larger for the highest redshift bin. In all three redshift bins, r_s is smaller for quiescent satellites than star-forming satellites. This is broadly in agreement with Chen (2008) and Prescott et al. (2011) who found the profile for blue satellites are shallower than red satellites.

Since we have extracted central galaxies in a fairly wide redshift range ($0.3 < z < 0.9$), it is natural for us to ask whether satellite number density distribution evolves with cosmic time. To estimate this, we plot the distributions from the three redshift bins on the same figure to compare (Figure 4.9, top panel). The number density of satellite galaxies increases significantly within 100kpc range, but remains almost the same on the outskirts.

Central galaxies were expected to grow through cosmic time via star-forming and merging with satellite galaxies. Therefore, a constant mass cut for centrals in three redshift bins may be inappropriate because we are not looking at the "same" population of galaxies at different stages (i.e., suffer from progenitor bias). Therefore, we also tried using evolving mass cut for central galaxies. We did not derive our own evolving mass cut as a function of redshift because this requires a good estimate of stellar mass function, which is beyond

the scope of this thesis. For this we took the equation from Tal et al. (2013) (which they derived from abundance matching of central galaxies) with a modification in the intercept of the linear relation of our evolving mass cut at different redshift ranges.

$$\log(M_{cen}/M_{\odot}) = -0.16z + 11.23 \tag{4.3.1}$$

The result using this evolving mass cut are plotted in Figure 4.9 (middle panel), we kept the same mass cut for satellites at $\log(M_{sat}/M_{\odot}) > 9.5$. Over time from $z = 0.9$ to $z = 0.3$, although the overall normalization and slope does not change significantly, satellites seem to pile up in inner region < 100kpc from central, making the distribution deviate more and more from an NFW profile. We also looked at redshift evolution for low-mass ($9.5 < \log(M_{sat}/M_{\odot}) < 10.2$) and high-mass ($10.2 < \log(M_{sat}/M_{\odot}) < \log(M_{cen}/M_{\odot})$) satellite galaxies separately (Figure 4.10). It is clear that most contribution of redshift evolution was from low-mass satellites.

In previous works, Tal et al. (2013) found no evolution in number density profile from $z = 1.6$ to $z = 0.04$. Nierenberg et al. (2012) also found no significant evolution from $z = 0.8$ to $z = 0.1$. Hartley et al. (2015) had the same central and satellite galaxy mass cut in two redshift bins ($0.4 < z < 1.3, 1.3 < z < 1.9$) and concluded that higher redshift centrals with same stellar mass cut have 50% more satellites due to higher halo masses. The sample selection methods are quite different. One big difference is that Tal et al. (2013) and

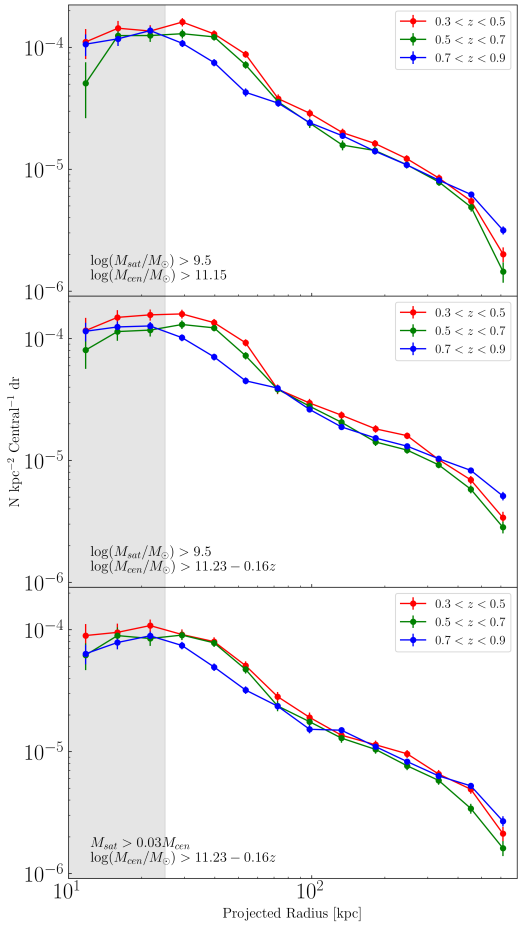

Figure 4.9: Evolution of satellite number density profile using different mass cuts in three redshift bins. Top Panel: The central galaxy mass cut is kept atlog$(M_{cen}/M_\odot) > 11.15$ in three redshift bins and mass cut for satellite galaxies were unchanged $\log(M_{sat}/M_\odot) > 9.5$. Middle Panel: The central galaxy mass cut followed Equation4.3.1, and mass cut for satellite galaxies is the same from top panel. Bottom Panel: The central galaxy mass cut followed Equation4.3.1 and satellite mass cut is relative to central mass $M_{sat} > 0.03M_{cen}$.

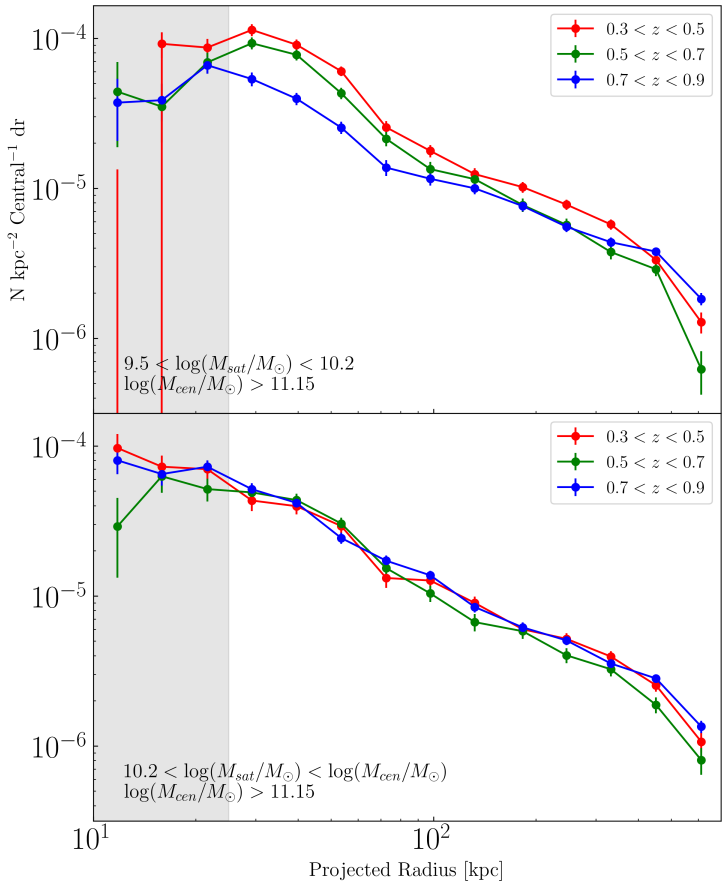

Figure 4.10: Evolution of satellite number density profile, split in two panels for low/high mass satellites. The central galaxy mass cut is kept at $\log(M_{cen}/M_\odot) > 11.15$ in all three redshift bins. Mass cut for satellite galaxies is $9.5 < \log(M_{sat}/M_\odot) < 10.2$ in top panel, and is $10.2 < \log(M_{sat}/M_\odot) < \log(M_{cen}/M_\odot)$ in bottom panel.

Nierenberg et al. (2012) used relative mass cut for satellite galaxies compared to central galaxy, while Hartley et al. (2015) and this thesis used a fixed satellite mass cut. The difference between Hartley et al. (2015) and this thesis is in sample selection and redshift range, which may explain different conclusions. We tested with a relative satellite mass cut at $M_{sat} > 0.03 M_{cen}$ in bottom panel of Figure 4.9, which shows that the previously found redshift evolution is not observable. We believe a fixed mass cut for satellites is more appropriate. Central galaxies grows over time through star-forming and mergers, but the satellites on average do not due to the fact that environmental effects tend to stop them from growing. Star-forming satellites do grow in mass, but certainly not at the same rate as the central galaxies. Therefore, in the sense of tracking same kind of satellite galaxies at different redshifts, using a fixed mass cut for satellites is more reasonable.

The redshift evolution of the distribution can be interpreted as a dynamical process of merging of satellites and infall of new satellites, while the surviving satellites migrate in the environment. Tal et al. (2013) interpreted their non-evolve result by stating that the merger rate and infall rate must have been equal. However, we found that this is probably only true for high-mass satellites (Figure 4.10). For low-mass satellites, the infall rate is higher than merger rate, as we observed number density build up for low-mass satellites.

Chapter 5

Discussion

5.1 Limitations and Caveats

There are some known caveats and limitations noted while our research was carried out. In this subsection we will discuss how these caveats influence our analysis and results.

5.1.1 Measurement Uncertainties

The magnitude measurement errors are relatively small and insignificant. Our photometric redshifts (photo-z's) have small uncertainties, the photo-z scatter is $\sigma_z = 0.044$ for faint objects in our sample. Since we used the same Δz cut for potential satellites and background objects, number counts of "true" satellite galaxies would not be affected significantly with a different scatter.

We also consider here the error in stellar mass and sfProb estimations. Our stellar mass estimation has about 30% uncertainty (1σ error given by LePhare, A. Golob, PhD thesis). Sobral et al. (2015); Sorba & Sawicki (2018) have shown that standard SED fitting underestimates stellar masses of star forming but not quiescent galaxies, which can cause a potential systematic bias in this thesis. In Figure 2.2, the sfProb distribution does not show a clear bimodal distribution as expected, indicating we have large uncertainties in sfProb. The main reason for this is that we used *ury* color criteria, which is a narrower wavelength range than the UVJ or $NUVrK$ diagram (Williams et al. 2009; Laigle et al. 2016; Moutard et al. 2016). However, we did not directly split the satellite galaxy sample according to sfProb value (instead we weighted our galaxy counts into two subsamples by sfProb). Thus we are less affected by the uncertainty of sfProb for individual galaxies, as star-forming and quiescent galaxy mass functions split by sfProb look consistent with traditional UVJ selections in Golob. et al. (in prep.). Adoption of the sfProb parameter may change the absolute value for our quiescent/star-forming related analysis, but the relative trend and comparison between the two subsamples were reasonable and trustable.

To test whether these caveats will affect our main conclusions, we perturbed mass and photo-z measurements and remeasured satellite number density profiles according to their associated uncertainties. We varied mass selection criteria and checked that profiles did not change significantly. The main features persist and our conclusions still hold given these uncertainties.

5.1.2 Selection Bias

In our sample selection process, we used mass selection and then applied isolation criteria to select massive central galaxies. We expect that they are very likely to be centrals in groups, but we do not confirm cluster or group membership for any galaxy. However, statistically our stacked satellite distribution can be interpreted as in a group-like environment.

Another bias we have is that we only observed relatively high mass satellite galaxies. Our conclusions hold for $\log(M_{sat}/M_{\odot}) > 9.5$ satellite galaxies but we cannot constrain distribution of less massive galaxies (there are presumably more of them at lower mass). Also, when counting satellite galaxies, we suffer from incompleteness within $\sim$20kpc from central galaxy, so we did not use that region to model the profiles. Light contamination and de-blending issues due to the central galaxy prevent us from detecting possible nearby satellites. In the future, modelling and subtracting central light would improve this situation.

5.2 Comparison with Studies in Literature

Due to in-homogeneities in data, sample selection and analysis methods, results from different studies are usually not directly comparable. In fact, some studies have opposite conclusions, especially on the dependence of the satellite distribution on central galaxy mass, satellite mass and redshift. Therefore, in the following subsections we only compare our

key results with literature results in a qualitative way.

5.2.1 Differences in analysis methods

Background contamination removal methods are different among papers, although the general idea is the same, which is to statistically account for the number density contribution from contamination objects due to the ambiguity of individual satellites' association with the centrals. Our method requires one random background aperture for each central galaxy unless no clean region is available (described in Section 3.1), following the method from Tal et al. (2012a) and Kawinwanichakij et al. (2014). Hartley et al. (2015) used a similar method but identified an additional source of contamination which is due to correlated background objects, and thus required random background measurements to be done within a few Mpc from the central. Guo et al. (2012) used a different approach and positioned the background measurements by using outer rings around host centrals. An alternative method was used by Nierenberg et al. 2012, who modeled both real satellites and background objects together, assuming the background is just a homogeneous and isotropic signal.

There is also no consensus on whether the distance from the central galaxy to the satellite galaxies should be scaled by r_{200}, the characteristic radius for clusters where the matter density is 200 times the mean density of the universe. Some authors scale and then stack while others directly stack profiles using physical scales without normalization. Hartley et al. (2015) pointed out that this scaling could be important. Ideally it would be better to

use r_{200} scales to consolidate scale dependent features. However, in practice a stellar-halo-mass relation (SHMR) is required for conversion from central galaxy stellar mass to r_{200} in observation. The reason for some not to scale is that there are uncertainties in stellar mass and in the relation between stellar mass and halo mass (Leauthaud et al. 2012b; Coupon et al. 2015) and could introduce an an additional source of uncertainty.

5.2.2 Do satellite galaxies follow the dark matter distribution?

According to the standard ΛCDM cosmological model, we would assume the galaxy clusters or groups are placed in massive host dark matter halos, in which there is a massive galaxy in the center and subhalos with their associated satellite galaxies orbit inside the dark matter halo (e.g. Mo et al. 2010). But questions concerning the relation between satellite galaxies dark matter halo still remain: do the satellites follow the dark matter distribution? Are they biased or unbiased tracers of matter distribution in general?

Generally, since satellite galaxies are thought to be associated to dark matter subhalos in the parent halo, they should follow the same distribution of subhalos, which is usually described by an NFW model (Ludlow et al. 2009). Wang et al. (2018) studied matter density distribution from a weak lensing study and number density profiles of galaxies in SDSS Stripe 82, and found that they have very similar concentration, both well fitted by the NFW profile. However, Watson et al. (2012) find that the profile of the low-luminosity satellite sample is consistent with NFW model, but the high-luminosity satellite sample has

a steeper inner slope than NFW. Piscionere et al. (2015) used clustering signal to measure the abundance of $M_r < -20$ satellite galaxies in SDSS DR7 data, and found that the radial number density profile is steeper than an NFW model in the inner regions within $\sim 50h^{-1}$ kpc.

Our result shows that in the $0.3 < z < 0.9$ redshift range, radial number density satellite distribution has an NFW shape on large radii, but is shallower than the predicted dark matter mass distribution, which indicates that satellites do not directly trace dark matter. Moreover, the observed distribution deviates from the NFW profile on small scales (within about 100kpc of the central galaxy). This feature agrees with Tal et al. (2012a); Watson et al. (2012); Piscionere et al. (2015) using SDSS data at low redshift, and indicates that on small scales, satellite galaxies follow a fundamentally different distribution from dark matter.

5.2.3 Quiescent fraction

Several papers reported that the quiescent fraction (fraction of quiescent satellites) of satellite galaxies has dependence on the projected distance to the central galaxy. Ann et al. (2008) found that morphology of satellite galaxy change with projected distance to central galaxy in SDSS DR5 data, as fraction of early type galaxies is higher close to the central galaxy. Prescott et al. (2011) studied red fraction in the satellites around isolated hosts at $0.01 < z < 0.15$ and found that the red fraction increases as radius decreases within a scale

of 200 kpc. Wang et al. (2014b) did not find a red fraction dependence on radius in their sample from SDSS DR8. Possible explanations for the discrepancy include different definitions of red/quiescent galaxies or selection bias. Our results agrees more with Prescott et al. (2011) as we found the quiescent fraction of satellites increases with decreasing radius around quiescent central galaxies, but no significant trend was found around star-forming centrals.

This quiescent fraction distance dependence can be explained by environmental quenching (Peng et al. 2010). When satellite galaxies fall close to the central galaxy, they experience stronger interaction with the central galaxy, and are more prone to be quenched through various processes. Under this assumption, one should expect the red fraction of satellite galaxies to increase when the distance to the central galaxy is reduced.

5.2.4 Galactic conformity

Weinmann et al. (2006) first systematically discovered galaxy conformity in SDSS data. Although different environment estimators should give different results, galaxy conformity was found repeatedly in the literature (e.g. Kauffmann et al. 2013; Hartley et al. 2015; Hearin et al. 2016). Our results show the fraction of quiescent satellite galaxies is indeed higher around quiescent central galaxies, indicating galaxy conformity and showing that it extends to at least $z = 0.8$.

There are multiple mechanisms proposed to explain the origin of galaxy conformity.

Hartley et al. (2015) concluded that mass of the dark matter halo only is not enough to explain galaxy conformity, and proposed an alternative mechanism related to gas outflow from the central galaxy. Physical origin of galaxy conformity may also come from the situation that if a central galaxy is star forming in a cluster, then the halo it lives in must have a large gas reservoir, which may serve to keep the satellite galaxies also star-forming. Hearin et al. (2016) explained origin of large-scale galaxy conformity by co-evolution of nearby dark matter halos (halo pair mutually evolving in the same large-scale tidal environment). They also showed that conformity should be undetectable at $z > 1$.

5.3 Comparison with Simulations

Simulations are helpful in probing physical mechanisms which shaped the number density distribution of satellites, as observations have limitations in directly measuring galaxy and dark matter properties, and also are not able to observe individual galaxies as they grow. In this subsection we will discuss whether the satellite distribution in simulations is directly comparable to observations.

Previous semi-analytic modeling (SAM) simulations usually found NFW-shaped satellite number density distributions, which is consistent with most observations (e.g. van den Bosch et al. 2005; Sales et al. 2007; Watson et al. 2012). However, they didn't observe the deviation from NFW profile of number density in inner regions. Using instead the full hydrodynamic simulation Illustris-1 (Vogelsberger et al. 2014), Brainerd (2018) found an

upward deviation from NFW model for radial number density profiles in the galaxy catalog. This analysis agrees with the deviation from NFW on small scales found in this thesis, despite the fact that mass distribution of satellite samples are very different. By comparing to the central galaxy mass density profile, Brainerd (2018) claimed that satellite number density distribution is shallower than the dark matter mass density profile. The different treatment of galaxy identification between SAM simulations and hydrodynamic simulations may be the reason why Brainerd (2018) gets results not seen in SAM simulations.

In this project, we used IllustrisTNG simulations (Nelson et al. 2018) to quantify simulated satellite distribution. IllustrisTNG is a suite of state-of-the-art hydrodynamic galaxy formation simulations with large box sizes of 110 (TNG100) and 302 (TNG300) comoving Mpc with a best mass resolution of 10^7 $M/M_\odot$ (TNGX00-1). Galaxies and dark matter halos are identified using the *Subfind* algorithm and saved in group catalogs. To validate the simulation data in comparison to observation, first we need to understand how well the simulation can recover the observed satellite number density distribution and its evolution.

We selected central and satellite galaxies in group catalogs provided by IllustrisTNG300-1 (Nelson et al. 2018). They were selected at snapshots 57 ($z = 0.76$) to 72 ($z = 0.4$), i.e., a similar redshift range as in our observations. Similar to the sample selection approach in our observational data, we adopted cylindrical shaped spatial selection in simulation with 700kpc radius and 700kpc difference cut on line-of-sight direction. Same stellar mass cut were also applied for central and satellite galaxies as in observation and isolation criteria for

central galaxy was applied in the 3D cylinder space. The difference between the observational data and the simulation is that no background subtraction and corrections of number counts are applied as the simulation does not suffer from these problems as do observation. In the meantime, we do need to tackle a few defects specific to the simulation, as we had to exclude some galaxies with artifacts.

We compared our results to Illustris-1 and the newly released IllustrisTNG300-1 simulation suite. We chose to perform the same analysis in TNG300-1 simulation because of its large box size ($\sim$ 300cMpc on one side) along with fine mass resolution ($\sim 10^7 M_\odot$). Satellite and central galaxy sample selection in simulation is kept as close as possible to what we did in observation. Figure 5.1 shows the comparison. The normalizations of the two profiles are similar, but the TNG satellite distribution (in blue) is steeper than the observed distribution (in black) and does not show as significant deviation from NFW profile on small scales. We decided to compare with Illustris as well because Brainerd (2018) saw the deviation-from-NFW feature in Illustris-1 despite different mass selection was used. We plotted results from the original Illustris simulation (in red, using the same selection and analysis), which followed similar shape on small scales to observation as it shows a deviation from NFW profile. However, it has a much smaller normalization (about 3 times fewer satellites) and does not agree with observation at $\sim$ 200 kpc.

We chose to move on with the TNG300-1 simulation because if its box size and fine mass resolution compared to Illustris-1. Difference between the two may be caused by

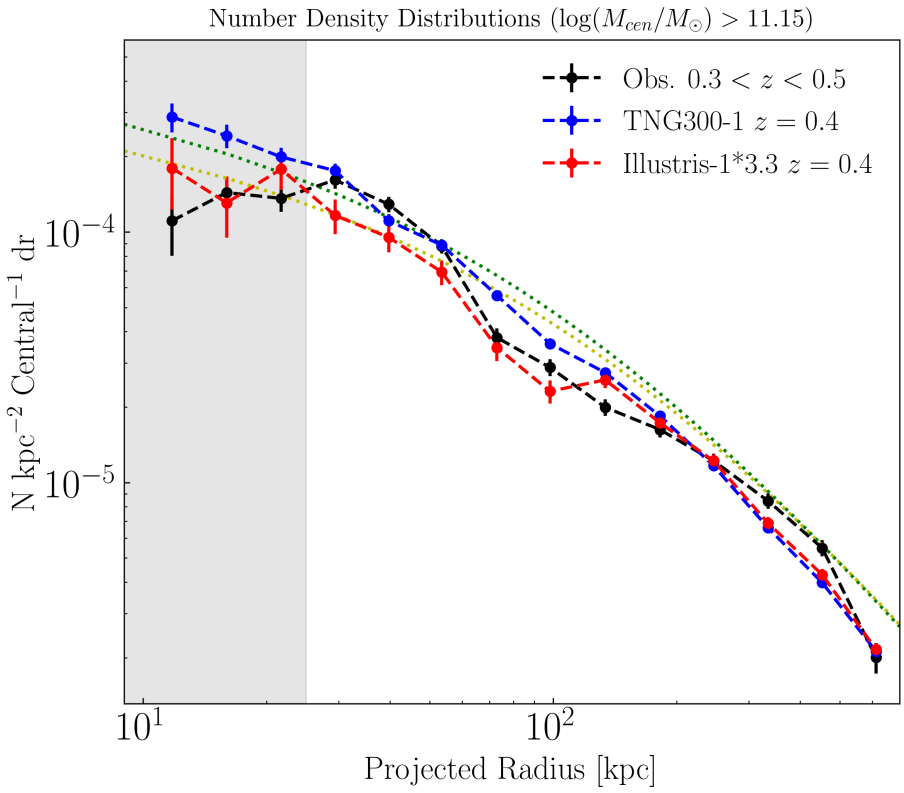

Figure 5.1: Comparison of satellite radial number density profiles between observation Illustris-1 and TNG300-1 results at $z \sim 0.4$. We renormalized Illustris satellite distribution to match the other two. We kept the same selection criteria or as close as we can for the three profiles (see text for description). The two dotted lines are the same in fig.4.1

difference in mass and force resolution, galaxy feedback etc. To see if better resolution would make a change, a future test should be done with TNG50 when it's released.

5.3.1 Redshift evolution

We selected central galaxies at three snapshots $z = 0.76, z = 0.6, z = 0.4$ (as the three redshift bin centers in our observation) in TNG300-1 and measured projected satellite number density distribution. We found that the redshift evolution does not agree with our observa-

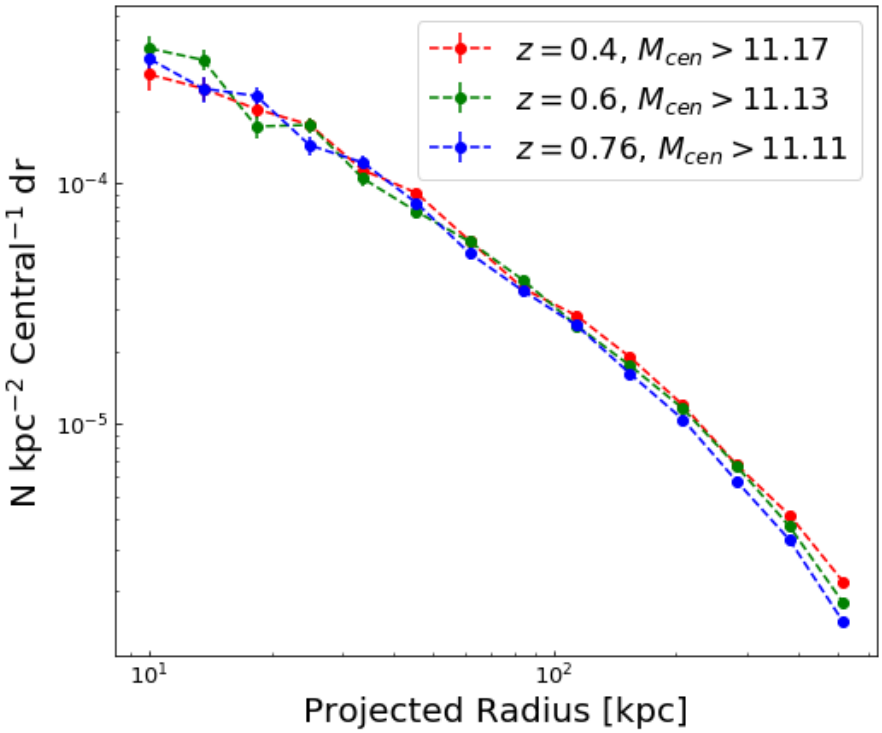

Figure 5.2: Redshift evolution of number density distribution of satellite galaxies in TNG300-1. The mass cut follows Equation 4.3.1 and satellites are selected using $\log(M_{sat}/M_{\odot}) > 9.5$.

tional results on small scales, but they qualitatively agree on large scales (Figure 5.2). With a constant mass cut, no evolution can be seen, but with an evolving mass cut, we do see some small growth in number density in the outskirts (similar to middle panel in Figure 4.9). But the deviation-from-NFW feature (described by Sersic profile in our observation) on small scale was not seen at the three snapshots in TNG300-1. If we instead track individual centrals and satellites over time (Figure 5.4), which we cannot do in the observations, we see a an inward migration of satellite galaxies.

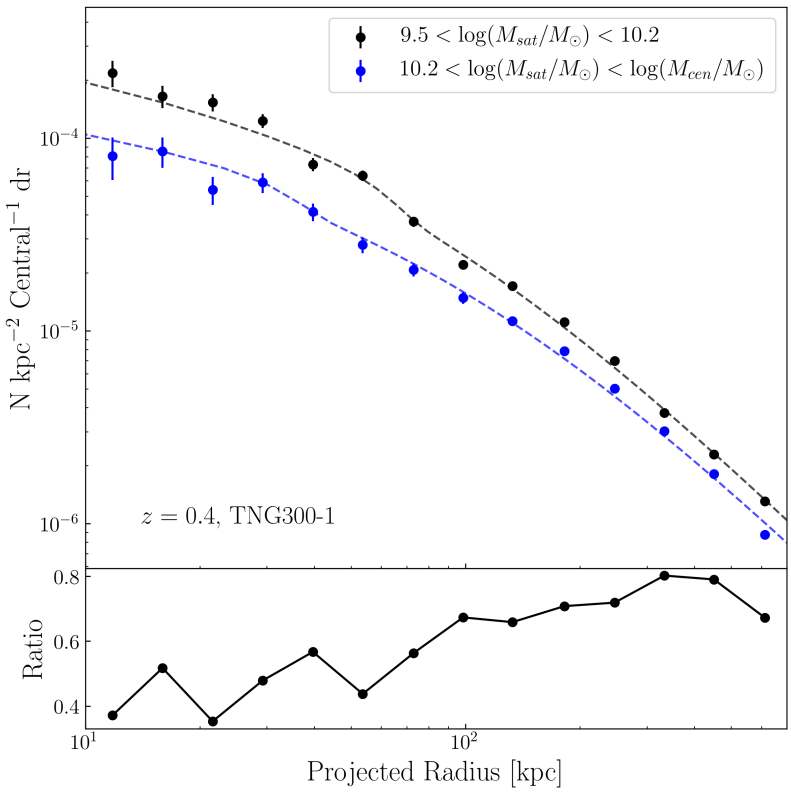

Figure 5.3: Radial number density of satellites in IllustrisTNG 300-1 simulation, split by stellar mass cut at $\log(M_{sat}/M_\odot) = 10.2$ at $z = 0.4$. Mass cut for central galaxy at $\log(M_{sat}/M_\odot) > 11.15$ was applied. The dash lines show NFW+Sersic fits in the top panel for the two distribution. Ratio to the two distribution is shown in the bottom panel.

5.3.2 Satellite mass dependence

We split satellite galaxies in TNG300-1 at $z = 0.4$ at the same mass cut $\log(M_{sat}/M_\odot) = 10.2$ as in the observed sample. The result (Figure 5.3) is in qualitative agreement with our observational results (Figure 4.7), where the concentration of low mass satellite galaxies is slightly greater than high mass satellite galaxies.

5.4 A Picture of the Formation of the Radial Satellite Number Density Distribution

If the stellar component in satellite galaxies and its dark matter subhalo act like test particles in dense environment, then their number density distribution should also follow the NFW profile (e.g. Ludlow et al. 2009). However, we observed an deviation feature from the NFW profile in inner regions ($\sim$ 100 kpc) in the distribution, extending to $0.3 < z < 0.9$ from earlier observations of this feature in SDSS data at low redshifts (Tal et al. 2012a; Watson et al. 2012; Piscionere et al. 2015).

Here we propose a possible explanation of the features observed in radial number density distribution of satellites where a combination of dynamical friction and tidal stripping is the main driver. When a low-mass dark matter halo with its associated galaxy falls within virial radius of a large parent halo (i.e., is accreted into the host dark matter halo), it becomes a subhalo. The subhalo along with its stellar component then feels strong dynamical friction and falls toward the central very quickly through orbital decay, meanwhile also suffering tidal stripping (Gao et al. 2004; Niemiec et al. 2017). Due to the dark matter subhalo being more extended than the stellar component, it is tidally stripped more strongly than the stellar matter, which means that the central stellar component remains largely unaffected while the dark matter subhalo loses mass. Once the satellite galaxy loses most of its dark matter halo due to tidal stripping, it does not lose as much velocity to dynamical friction

as before because the remaining core of dark matter subhalo and the stellar component is more compact and experiences less friction.

The proposed scenario could cause the satellites to pile up where the transition of strength of dynamical friction and tidal stripping happens, as we observed some deviation from NFW profile and saw redshift evolution enhances number density of satellites mainly on small scales. We also require the stripping strength should have a strong increase around 100 kpc for this scenario to be consistent with the excess of satellites over NFW profile, or the dark matter subhalo should be almost completely stripped at such distance.

We found that the build-up process of number density that we discussed in section 4.3 is only significant for low mass satellites. This mass dependence implied by our result is consistent with the close-pair merging timescale estimated by Kitzbichler & White (2008) and Jiang et al. (2008), who found larger mass companion galaxies have shorter merging timescales with the central galaxy. The dependence of satellite radial distribution profile on satellite mass is new evidence that the process governing the distribution is mass dependent, consistent with dynamical friction being stronger for small satellites. Tal et al. (2013) explained number density redshift evolution as a dynamical process and found a balance between merging and replenishment. However, based on the mass dependence we found, the balance is true only for high mass satellites; for low-mass satellites, replenishment rate is higher than merging rate, thus an increase of number density through time is observed for low-mass satellites. A drawback for our interpretation is that we did not observe mass

segregation on large scales, which one might expect from mass dependence of dynamical friction. This could be due to dynamical friction being not the dominant mechanism on large scales.

We tested this evolution scenario with IllustrisTNG simulation by tracking individual satellites through cosmic time to see the environmental effects on their migration (Section 5.4.1), and we recovered features of dynamical friction and tidal stripping, although the deviation from NFW was not observed in TNG simulation. Future measurements on the velocities of the satellite galaxies and mass measurement of the dark matter parent halo and subhalos may be able to further test this scenario.

5.4.1 Test of the migration scenario with simulation

To test the satellite migration scenario, we again turn to the Illustris TNG300-1 simulation to track how individual satellites migrate. For the purpose of testing the scenario, we need to investigate how this migration is related to dynamical friction and tidal stripping.

To quantify migration of satellites, it is essential that we are able to track individual subhalos and galaxies through snapshots using *Sublink* merger trees provided with the group catalogs. In Figure 5.8, we show distance distribution of satellites, color-coded by different fates at $z = 0$. It is clear that satellite galaxies that merged after we start tracking them were already close to the center at snap 57 ($z = 0.76$). Moreover, we observed a mass dependence of merging fraction and it is higher for high mass satellites, the difference is especially sig-

nificant at 50-200 kpc . Combined with satellite mass dependence of the redshift evolution figure (Figure 4.10), this indicates that the merging-replenishment balance (as proposed in Tal et al. 2013) may only be valid for low-mass satellites.

To avoid confusion and complexity, we only track satellite galaxies with a well-defined main descendant branch, and therefore we essentially track the galaxies which do not experience a merger event or only merged with less massive satellites until $z = 0$ (hereafter "survived satellites").

We first select central galaxies and associated satellite galaxies in TNG300-1 at snapshot 57 ($z = 0.76$) and ask where these satellites are relative to the centrals in later snapshots until snapshot 72 ($z = 0.4$). Then we quantify the radial distribution for those satellite galaxies at different snapshots (Figure 5.4). A pile-up process of satellite galaxies is clearly visible on $\sim$100 kpc scale. This indicates that migration of satellite galaxies can contribute to the pile-up process we observed. Note that, in contrast to observations, in the simulation we actually track the same satellite galaxies (except those merged or disrupted) through redshift and watched the number density building up close to the center, rather than sampling at different redshifts, and yet we are able to recover the build-up process.

To directly investigate migration of satellites on different scales, we looked at how radial distance of individual satellites change through time (shown in Figure 5.5) by measuring distance ratio between snapshot 57 ($z = 0.76$) and 72 ($z = 0.4$). Here only satellite galaxies that survived during the tracking period are shown, and the two curves represent a non-

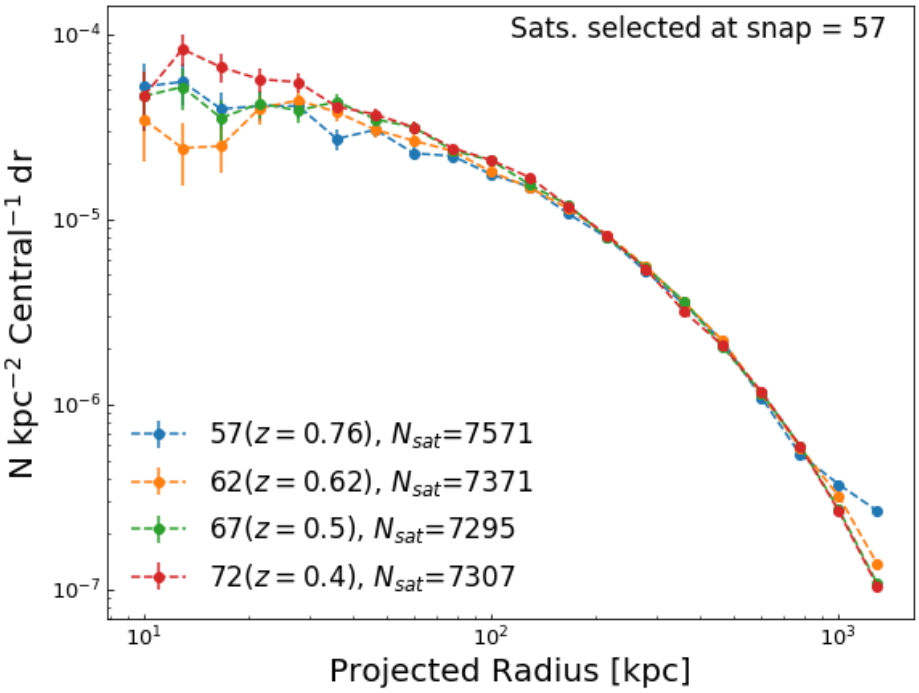

Figure 5.4: Evolution of radial satellite number density distribution in TNG300-1 simulation, tracking satellites selected at $z = 0.76$ (snap 57) to $z = 0.4$(snap 72).

parametric fit to the general trend for high and low mass satellites. We found that most of the satellites move inward if they started on large scales at snapshot 57. The radius ratio at two snapshots depends on the radius at beginning time, as satellites at outskirts have a smaller ratio and satellites close to the center have close-to-one radius ratio or larger-than-one ratio. We find this migration process is slightly mass dependent. This can be explained by dynamical friction as it slows down galaxies and sink them towards the center, and more massive subhalos suffer more deceleration from friction.

To investigate tidal stripping, subhalo mass changes for individual satellites between two snapshots (72 and 57) were also tracked for the satellites (Figure 5.6). Figure 5.6 shows that tidal stripping is happening to satellite galaxies when they migrate, as most satellite galaxies lose their dark matter halo mass from snapshot 57 to snapshot 72. However, their stellar mass is mostly unaffected or grows if the satellites were star-forming (Figure 5.7). Quiescent satellite galaxies have smaller subhalo masses because they are closer to the center and thus have already experienced large amount of stripping when we first start tracking them at snap 57 ($z = 0.76$).

These results confirmed that most satellite galaxies move inward once they fall close to central galaxy and more massive satellites move quicker towards the central, while tidal stripping is also in place. However, the fact that the simulation did not recover the two-component radial number density distribution for satellites shows that there are fundamental differences in the simulation and our observation. Therefore, despite the success of the

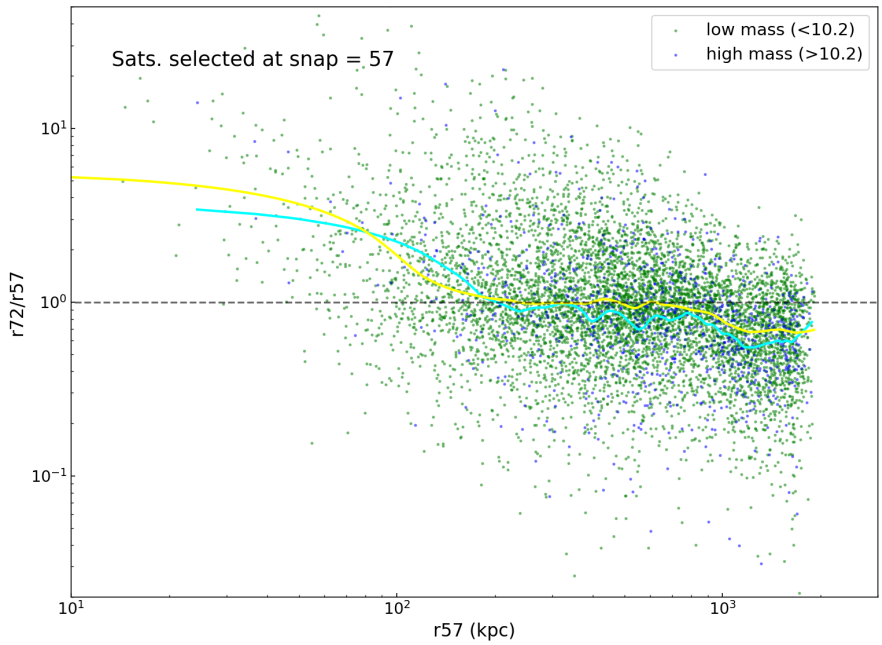

Figure 5.5: Distance change of survived satellite galaxies from $z = 0.76$ to $z = 0.4$ in TNG300-1 simulation, tracking satellites selected at $z = 0.76$ (snap 57). The cyan and yellow curve show non-parametric fitting for the high mass and low mass satellites respectively.

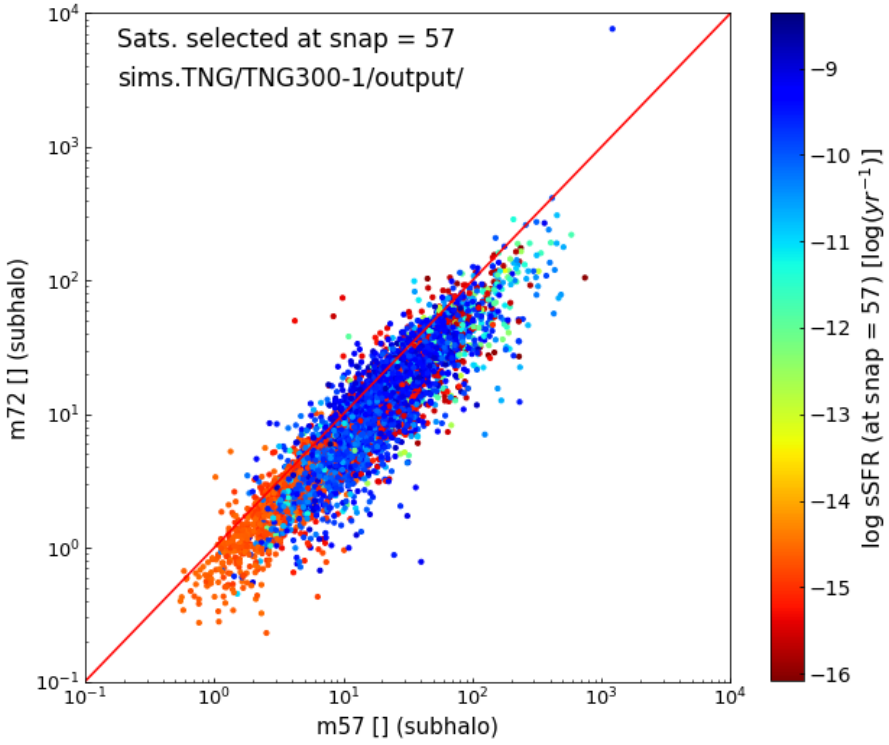

Figure 5.6: Subhalo mass change of survived satellite galaxies from $z = 0.76$ to $z = 0.4$ in TNG300-1 simulation..

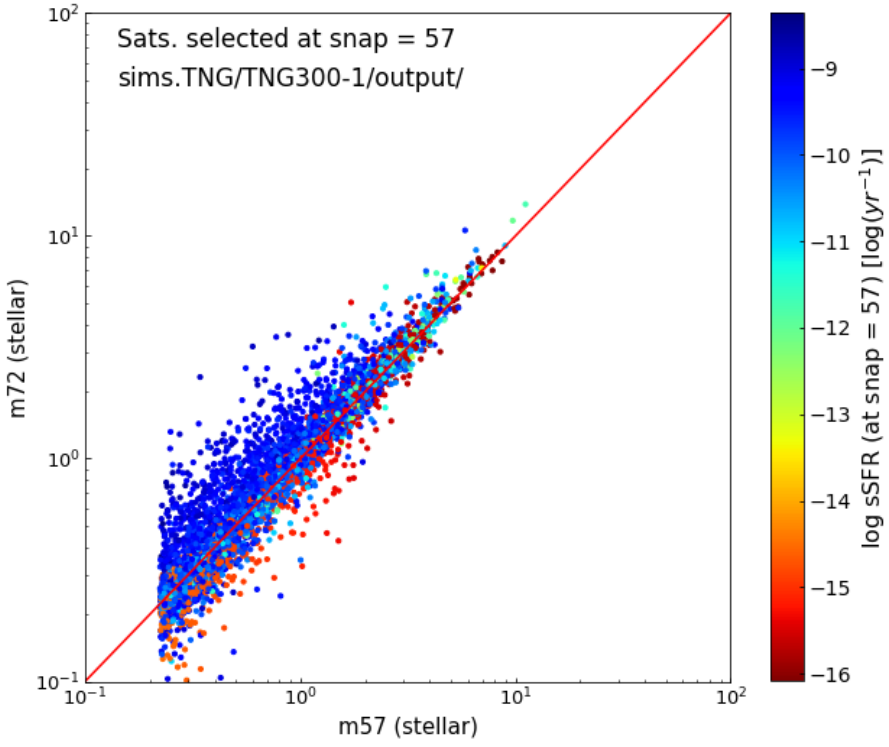

Figure 5.7: Stellar mass change of survived satellite galaxies from $z = 0.76$ to $z = 0.4$ in TNG300-1 simulation..

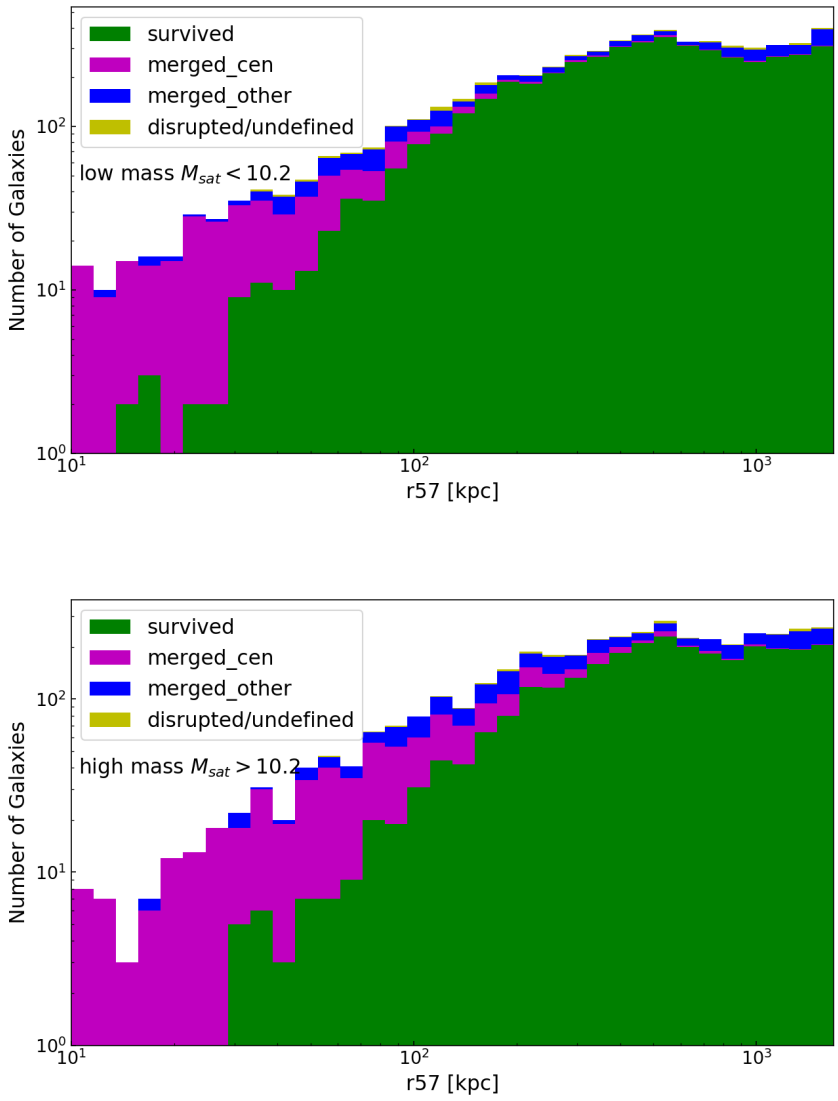

Figure 5.8: Number of TNG300-1 satellite galaxies as a function of their distance at snap 57 ($z = 0.76$), color coded by their fate at $z = 0$. In each panel, green, magenta/blue and yellow histograms show survived, merged, and disrupted (or not defined in any merger tree) satellite galaxies separately. Top panel and bottom panel show the low mass and high mass satellites respectively.

simulation in confirming the existence of dynamical friction and tidal stripping, we have to keep in mind that simulation has its own defects and may not represent the same physical processes that happen in real universe.

Chapter 6

Conclusions

Using deep and wide surveys, Subaru-HSC-SSP and CFHT-CLAUDS, we measured radial number density distribution of satellite galaxies in the redshift range $0.3 < z < 0.9$ around massive central galaxies with $\log(M_{cen}/M_{\odot}) > 11.15$. We also investigated how the radial number density of satellites depends on satellite mass/star-formation activity, central mass/star-formation activity, and whether it evolves with cosmic time. We find the following features in the number density distribution of our satellite galaxy sample:

1. Within our redshift range $0.3 < z < 0.9$, the satellite radial number density distributions are well described by NFW profile at large radius to central galaxy (> 100kpc), but we observe a deviation of number density distribution from NFW profile close to central galaxy (~ 100kpc), which is present throughout the whole redshift range and is the first time it is seen at these redshifts. .

2. We investigated redshift evolution of radial satellite number density distribution by looking at the distribution in three redshift bins form $z = 0.9$ to $z = 0.3$. Either with or without an evolving mass cut for central galaxies (to keep up with mass growth of centrals over time), we observed a build-up of the number density of satellites within $\sim$100 kpc, indicating that satellite galaxies were migrating inwards, while the normalization and slope does not change significantly on the outskirts. Moreover, we found that most contribution of build-up of number density is from low mass satellites. The number density of high mass satellites barely grows, suggesting higher merger rate for high mass satellites.

3. Satellites in two different mass bins have distributions of similar concentration. However, on small scales, the significance of the deviation from the NFW profile is greater for low-mass satellites than for high-mass satellites. We also found that quiescent fraction of satellites decreases with decreasing satellite stellar mass, which is consistent with the trend in field galaxies.

4. Dividing the central galaxy sample by stellar mass, we found that higher-mass central galaxies have more satellite galaxies on average. We did not find significant difference in concentration (parameterized by characteristic radius) for satellite distributions around centrals with different masses.

5. Dividing the central galaxy sample by star-formation activity, we found that galaxy

conformity signal exists up to $z = 0.9$, where only around quiescent centrals the quiescent fraction of satellites is above field level. This confirms findings from Hartley et al. (2015); Kawinwanichakij et al. (2016).

6. We proposed a physical interpretation for the two-component radial distribution for satellites, in which tidal stripping and dynamical friction are the main processes in shaping the distribution.

In summary, we recovered some features in radial number density in the literature, including galactic conformity and the feature that number of satellites increasing with central mass. We also extended discovery of the deviation-from-NFW feature to intermediate redshift for the first time and proposed an interpretation. The fact that it is hard to compare with the literature shows that to reach a solid consensus, a more consistent sample selection is necessary. Future work will be needed on confirming physical interpretations, for which better simulation would definitely help. Spectroscopic confirmation of membership and a sample in higher redshift would certainly be helpful.

Appendix A

Sample selection test

A.1 Background Subtraction Method Test

Since background objects do not cluster around central galaxies, they are supposed to have a uniform distribution, thus if potential satellites and background were plotted in our figures separately, the distribution background objects should be flat. We confirmed this in Figure A.1

A.2 Satellite Selection Redshift Cut

We tested what is the best range of redshift difference from central to include most potential satellite galaxies (i.e. maximize completeness). We tried different cuts $n\sigma_z$ for $n = 1.5, 3, 4.5, 6, 9$ and found that 4.5 is big enough to include most potential satellites

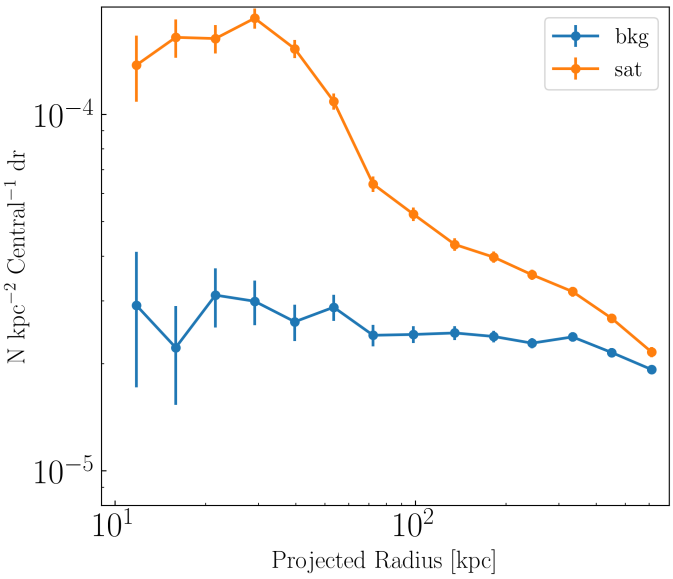

Figure A.1: Radial Number Distribution of Potential Satellites (not background corrected) and Background Objects at $0.3 < z < 0.5$.

because number density starts to converge if we keep using larger redshift cuts. Using a bigger redshift cut enables us to quantify satellites better on small scales as it suffer less from background objects than number density estimate on large scales (see Figure A.1 for example).

A.2.1 Result Figures using another redshift cut

For comparison, we show the results using $1.5\sigma_z$ as a redshift cut for isolation criteria (Section 2.2.1) and potential satellite selection (Section 2.2.2). Here we did not remove overlap regions between SXDS field and XMM field, but since the overlap region is small and only less than 5% central galaxies are in that region, the results are not affected.

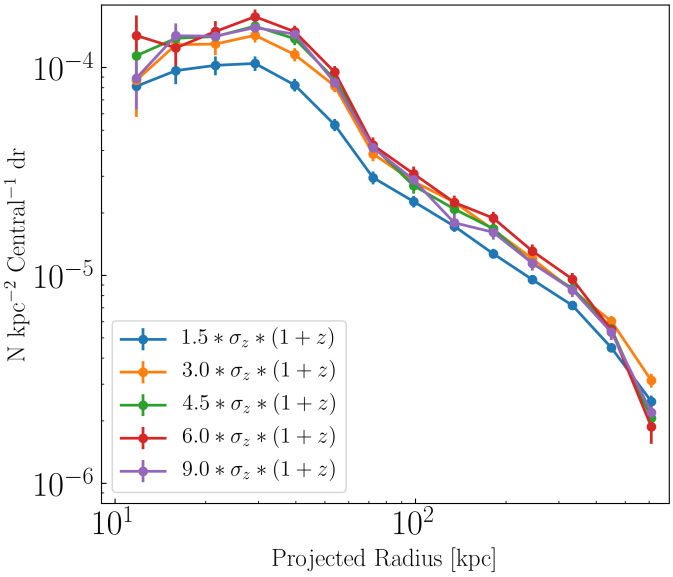

Figure A.2: Test of Redshift Cut in Satellite Selection.

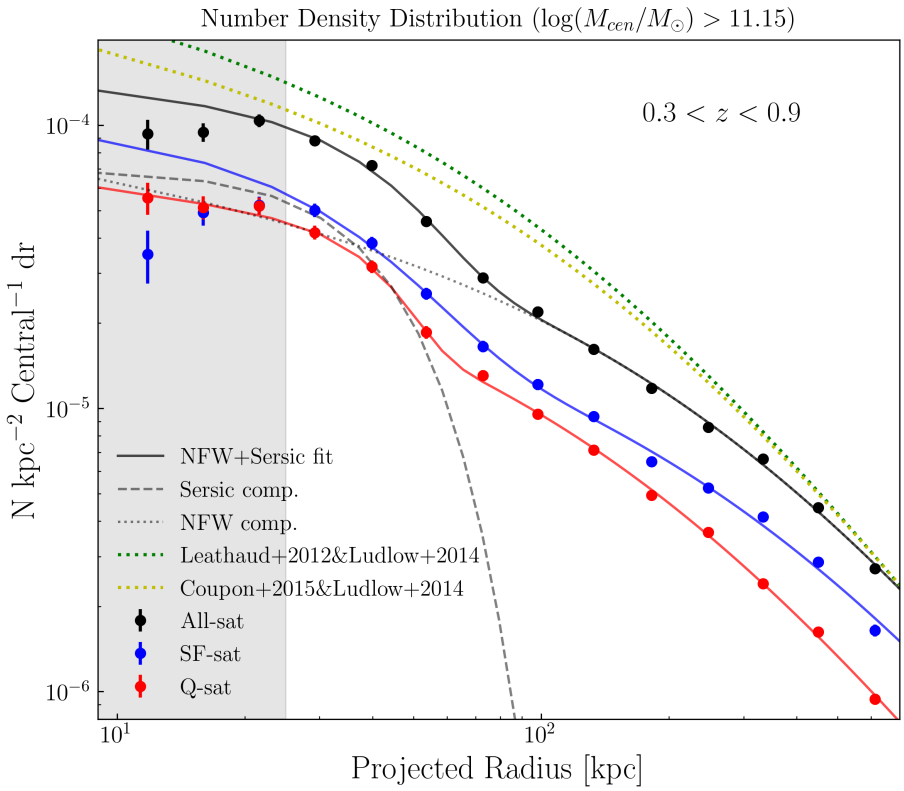

Figure A.3: Same as Figure 4.1, but using a $1.5\sigma_z$ redshift cut for isolation criteria and satellite selection.

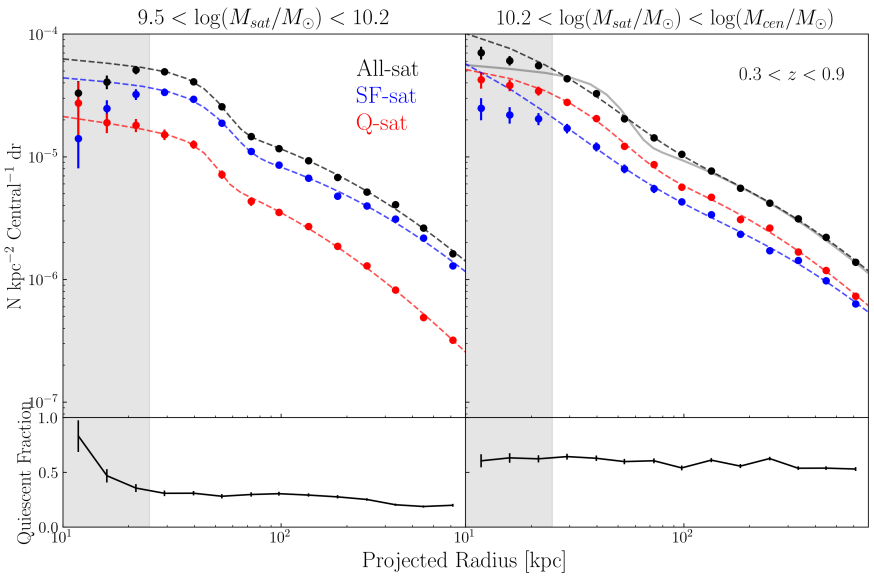

Figure A.4: Same as Figure 4.7, but using a $1.5\sigma_z$ redshift cut for isolation criteria and satellite selection.

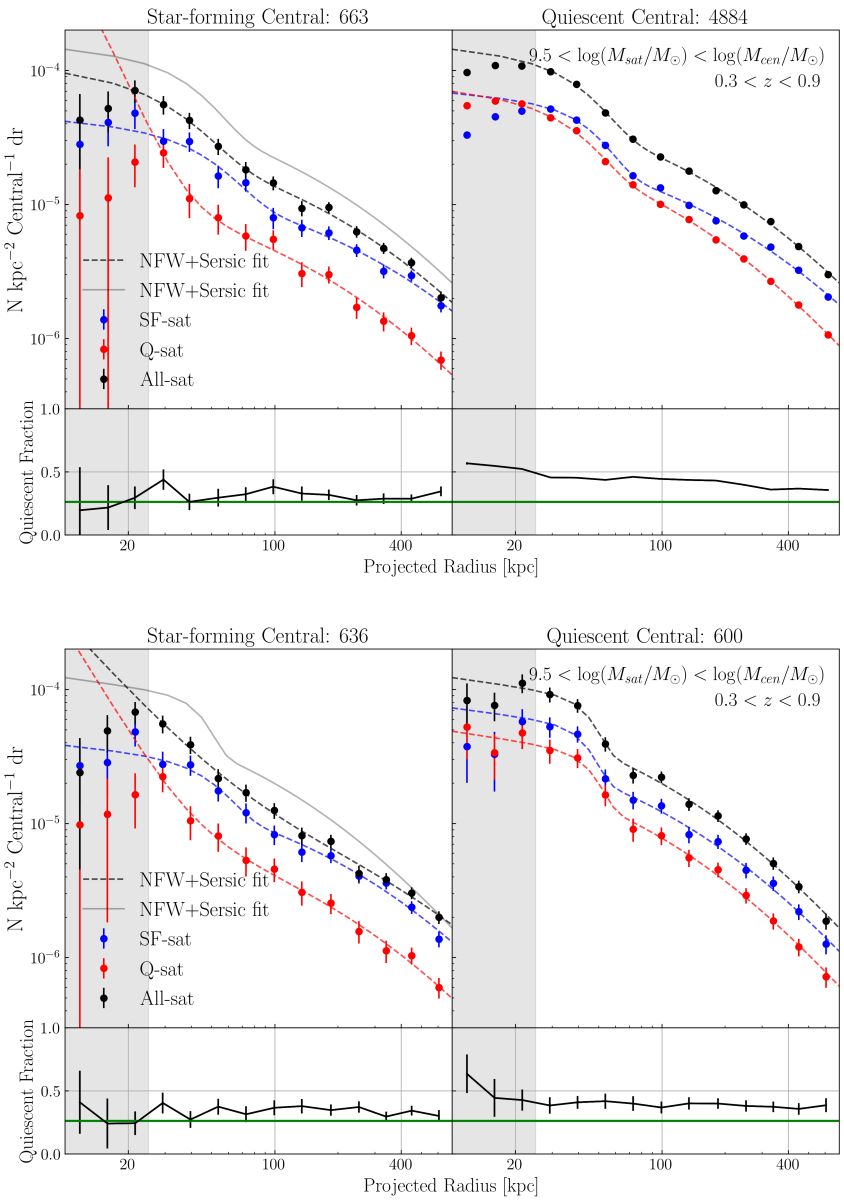

Figure A.5: Same as Figure 4.3, but using a $1.5\sigma_z$ redshift cut for isolation criteria and satellite selection.

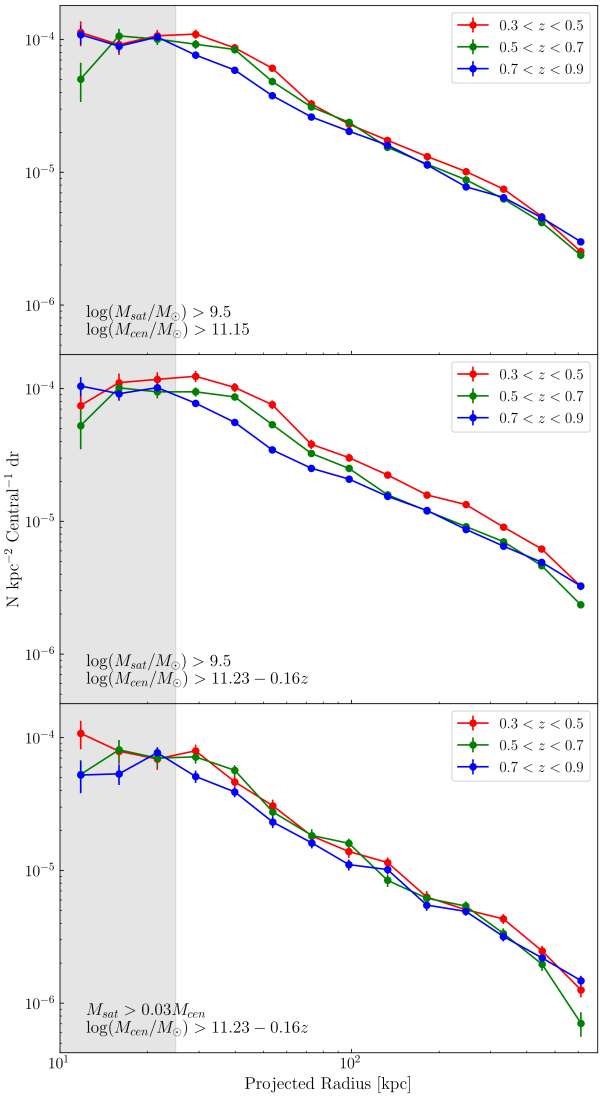

Figure A.6: Same as Figure 4.9, but using a $1.5\sigma_z$ redshift cut for isolation criteria and satellite selection.

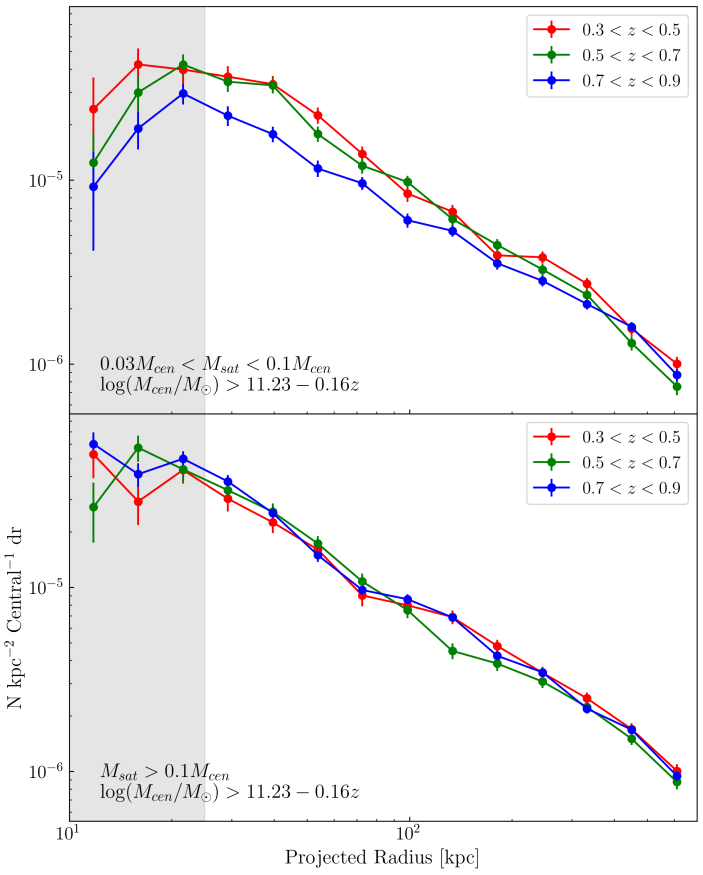

Figure A.7: Same as Figure 4.10, but using a $1.5\sigma_z$ redshift cut for isolation criteria and satellite selection.

Bibliography

Aihara, H., Arimoto, N., Armstrong, R., et al. 2018, Publications of the Astronomical Society of Japan, 70, 50

Ann, H. B., Park, C., & Choi, Y. Y. 2008, Monthly Notices of the Royal Astronomical Society, 389, 86

Arnouts, S., Cristiani, S., Moscardini, L., et al. 1999, Monthly Notices of the Royal Astronomical Society, 310, 540

Arnouts, S., Le Floc'H, E., Chevallard, J., et al. 2013, Astronomy and Astrophysics, 558, A67

Balogh, M., Eke, V., Miller, C., et al. 2004, Monthly Notices of the Royal Astronomical Society, 348, 1355

Balogh, M. L., Morris, S. L., Yee, H. K. C., Carlberg, R. G., & Ellingson, E. 1999, The Astrophysical Journal, 527, 54

Barsanti, S., Owers, M. S., Brough, S., et al. 2018, The Astrophysical Journal, 857, 71

Bartelmann, M. 1996, Astronomy & Astrophysics, 313, 697

Bertin, E. & Arnouts, S. 1996, Astronomy and Astrophysics Supplement Series, 117, 393

Binney, J. & Tremaine, S. 1987, Galactic Dynamics (Princeton University Press), 747

Boselli, A. & Gavazzi, G. 2006, Publications of the Astronomical Society of the Pacific, 118, 517

Brainerd, T. G. 2018, The Astrophysical Journal, 868, L7

Bruzual, G. & Charlot, S. 2003, Monthly Notices of the Royal Astronomical Society, 344, 1000

Budzynski, J. M., Koposov, S. E., Mccarthy, I. G., Mcgee, S. L., & Belokurov, V. 2012, Monthly Notices of the Royal Astronomical Society, 423, 104

Calzetti, D., Armus, L., Bohlin, R. C., et al. 2000, The Astrophysical Journal, 533, 682

Chandrasekhar, S. 1943, The Astrophysical Journal, 97, 255

Chen, J. 2008, Astronomy & Astrophysics, 484, 347

Collister, A. A. & Lahav, O. 2005, Monthly Notices of the Royal Astronomical Society, 361, 415

Coupon, J., Arnouts, S., van Waerbeke, L., et al. 2015, Monthly Notices of the Royal Astronomical Society, 449, 1352

Davidzon, I., Ilbert, O., Laigle, C., et al. 2017, Astronomy & Astrophysics, 605, A70

Dressler, A., Oemler, A., Couch, W. J., et al. 1997, The Astrophysical Journal, 490, 577

Fossati, M., Wilman, D. J., Mendel, J. T., et al. 2017, The Astrophysical Journal, 835, 153

Gao, L., White, S. D., Jenkins, A., Stoehr, F., & Springel, V. 2004, Monthly Notices of the Royal Astronomical Society, 355, 819

Gómez-Guijarro, C., Toft, S., Karim, A., et al. 2018, The Astrophysical Journal, 856, 121

Gunn, J. & Gott, J. R. 1972, Astrophysical Journal, 176, 1

Guo, Q., Cole, S., Eke, V., & Frenk, C. 2012, Monthly Notices of the Royal Astronomical Society, 427, 428

Guo, Y., Bell, E. F., Lu, Y., et al. 2017, The Astrophysical Journal, 841, L22

Hartley, W. G., Conselice, C. J., Mortlock, A., Foucaud, S., & Simpson, C. 2015, Monthly Notices of the Royal Astronomical Society, 451, 1613

Hashimoto, Y., Oemler, Jr., A., Lin, H., & Tucker, D. L. 1998, The Astrophysical Journal, 499, 589

Hatfield, P. W. & Jarvis, M. J. 2016, MNRAS, 472, 3570

Hearin, A. P., Behroozi, P. S., & van den Bosch, F. C. 2016, Monthly Notices of the Royal Astronomical Society, 461, 2135

Hinshaw, G., Larson, D., Komatsu, E., et al. 2013, Astrophysical Journal, Supplement Series, 208, 19

Huang, J. S., Faber, S. M., Willmer, C. N., et al. 2013, Astrophysical Journal, 766, 21

Jiang, C. Y., Jing, Y. P., Faltenbacher, A., Lin, W. P., & Li, C. 2008, The Astrophysical Journal, 675, 1095

Kauffmann, G., Li, C., Zhang, W., & Weinmann, S. 2013, Monthly Notices of the Royal Astronomical Society, 430, 1447

Kawinwanichakij, L., Papovich, C., Quadri, R. F., et al. 2014, Astrophysical Journal, 792

Kawinwanichakij, L., Quadri, R. F., Papovich, C., et al. 2016, The Astrophysical Journal, 817, 9

Kitzbichler, M. G. & White, S. D. M. 2008, Monthly Notices of the Royal Astronomical Society, 391, 1489

Kovač, K., Lilly, S. J., Knobel, C., et al. 2014, Monthly Notices of the Royal Astronomical Society, 438, 717

Laigle, C., Mccracken, H. J., Ilbert, O., et al. 2016, The Astrophysical Journal Supplement Series, 224, 1

Lares, M., Lambas, D. G., & Domínguez, M. J. 2011, Astronomical Journal, 142, 13

Leauthaud, A., Tinker, J., Bundy, K., et al. 2012a, The Astrophysical Journal, 744, 159

Leauthaud, A., Tinker, J., Bundy, K., et al. 2012b, Astrophysical Journal, 744

Ludlow, A. D., Navarro, J. F., Angulo, R. E., et al. 2014, Monthly Notices of the Royal Astronomical Society, 441, 378

Ludlow, A. D., Navarro, J. F., Springel, V., et al. 2009, Astrophysical Journal, 692, 931

Malavasi, N., Pozzetti, L., Cucciati, O., Bardelli, S., & Cimatti, A. 2015, Astronomy & Astrophysics, 585, A116

Mo, H., van den Bosch, F. C., & White, S. 2010, Galaxy Formation and Evolution, Vol. 1 (Cambridge University Press), 740

Moore, B., Katz, N., Lake, G., Dressler, A., & Oemler, A. 1996, Nature, 379, 613

Moutard, T., Arnouts, S., Ilbert, O., et al. 2016, Astronomy and Astrophysics, 590, A103

Moutard, T., Sawicki, M., Arnouts, S., et al. 2018, Monthly Notices of the Royal Astronomical Society, 479, 2147

Navarro, J. F., Frenk, C. S., & White, S. D. M. 1995, The Astrophysical Journal, 462, 563

Nelson, D., Springel, V., Pillepich, A., et al. 2018, ArXiv, 1812.05609

Niemi, S. M., Heinämäki, P., Nurmi, P., & Saar, E. 2010, Monthly Notices of the Royal Astronomical Society, 405, 477

Niemiec, A., Jullo, E., Limousin, M., et al. 2017, Monthly Notices of the Royal Astronomical Society, 471, 1153

Nierenberg, A. M., Auger, M. W., Treu, T., Marshall, P. J., & Fassnacht, C. D. 2011, Astrophysical Journal, 731

Nierenberg, A. M., Auger, M. W., Treu, T., et al. 2012, Astrophysical Journal, 752, 99

Oemler, Augustus, J. 1974, The Astrophysical Journal, 194, 1

Peng, Y. J., Lilly, S. J., Kovač, K., et al. 2010, Astrophysical Journal, 721, 193

Piscionere, J. A., Berlind, A. A., McBride, C. K., & Scoccimarro, R. 2015, Astrophysical Journal, 806, 125

Postman, M. & Geller, M. J. 1984, The Astrophysical Journal, 281, 95

Prescott, M., Baldry, I. K., James, P. A., et al. 2011, Monthly Notices of the Royal Astronomical Society, 417, 1374

Prevot, M., Lequeux, J., MAURICE, E., Prevot, L., & Rocca-Volmerange, B. 1984, Astronomy and Astrophysics, 132, 389

Read, J. I., Wilkinson, M. I., Evans, N. W., Gilmore, G., & Kleyna, J. T. 2006, Monthly Notices of the Royal Astronomical Society, 366, 429

Salerno, J. M., Martínez, H. J., & Muriel, H. 2019, Monthly Notices of the Royal Astronomical Society, 484, 2

Sales, L. V., Navarro, J. F., Lambas, D. G., White, S. D. M., & Croton, D. J. 2007, Monthly Notices of the Royal Astronomical Society, 382, 1901

Sarkar, S. & Pandey, B. 2019, Monthly Notices of the Royal Astronomical Society, 485, 4743

Sawicki, M., Arnouts, S., Huang, J., et al. 2019, MNRAS, 0, 0

Sérsic, J. L. 1963, Boletin de la Asociacion Argentina de Astronomia La Plata Argentina, 6, 41

Smith, R. J., Lucey, J. R., Price, J., Hudson, M. J., & Phillipps, S. 2012, Monthly Notices of the Royal Astronomical Society, 419, 3167

Sobral, D., Matthee, J., Darvish, B., et al. 2015, The Astrophysical Journal, 808, 139

Somerville, R. S. & Davé, R. 2015, Annu. Rev. Astron. Astrophys, 53, 51

Sorba, R. & Sawicki, M. 2018, Monthly Notices of the Royal Astronomical Society, 476, 1532

Springel, V., White, S. D. M., Jenkins, A., et al. 2005, Nature, 435, 629

Tal, T., Van Dokkum, P. G., Franx, M., et al. 2013, Astrophysical Journal, 769, 31

Tal, T., Wake, D. A., & Van Dokkum, P. G. 2012a, Astrophysical Journal Letters, 751, L5

Tal, T., Wake, D. A., Van Dokkum, P. G., et al. 2012b, Astrophysical Journal, 746, 138

Tollet, ., Cattaneo, A., Mamon, G. A., Moutard, T., & van den Bosch, F. C. 2017, Monthly Notices of the Royal Astronomical Society, 471, 4170

Trujillo, I., Carretero, C., & Patiri, S. G. 2006, The Astrophysical Journal, 640, 111

van den Bosch, F. C., Yang, X., Mo, H. J., & Norberg, P. 2005, Monthly Notices of the Royal Astronomical Society, 356, 1233

Vogelsberger, M., Genel, S., Springel, V., et al. 2014, Nature, 509, 177

Vulcani, B., Marchesini, D., De Lucia, G., et al. 2016, The Astrophysical Journal, 816, 86

Wang, C., Li, R., Gao, L., et al. 2018, Monthly Notices of the Royal Astronomical Society, 475, 4020

Wang, H., Mo, H. J., Yang, X., Jing, Y. P., & Lin, W. P. 2014a, The Astrophysical Journal, 794, 94

Wang, W., Sales, L. V., Henriques, B. M. B., & White, S. D. M. 2014b, Monthly Notices of the Royal Astronomical Society, 442, 1363

Watson, D. F., Berlind, A. A., McBride, C. K., Hogg, D. W., & Jiang, T. 2012, Astrophysical Journal, 749, 83

Weinmann, S. M., Kauffmann, G., Van Den Bosch, F. C., et al. 2009, Monthly Notices of the Royal Astronomical Society, 394, 1213

Weinmann, S. M., Van Den Bosch, F. C., Yang, X., & Mo, H. J. 2006, Monthly Notices of the Royal Astronomical Society, 366, 2

Wetzel, A. R., Tinker, J. L., & Conroy, C. 2012, Monthly Notices of the Royal Astronomical Society, 424, 232

Williams, R. J., Quadri, R. F., Franx, M., Van Dokkum, P., & Labbé, I. 2009, Astrophysical Journal, 691, 1879

Zehavi, I., Weinberg, D. H., Zheng, Z., et al. 2004, The Astrophysical Journal, 608, 16